Toward Realistic Full Cells with Protected Lithium-Metal-Anodes: the Effect of an Adaptive Self-healing Artificial SEI

Stephan Burger, Julian Skrotzki, Jan Büttner, Witali Beichel,* Petra Klose, Alexander Welle, Anna Fischer, and Ingo Krossing*

The application of an artificial LiBFEP-SEI on thin 48 μm Lithium-Metal-Anodes (LiBFEP = Li[O$_2$P(OCH$_2$CF$_3$)$_2$]; SEI = solid electrolyte interphase) induces improved plating/stripping of lithium at the interphase with an almost doubling of the lifetime for Li–Li symmetrical cells. Four lithium-fluoroalkylphosphates other than LiBFEP are tested, but all perform inferior to the control. Lithium-metal full cells with various NMC-cathodes and LP57 standard electrolyte are employed to confirm the superior performance of the LiBFEP artificial SEI (LP57 = 1 M Li[PF$_6$] in ethylene carbonate/ethyl methyl carbonate 3:7 wt%). A tripling of the cell lifetime is observed using realistic cell-cycle parameters. The stabilization of the modified anodes is evidenced by SEM-EDX, ToF-SIMS, PEIS measurements and led to an improved anode structure. The performance of the artificial SEI is further improved with the introduction of a novel low-concentration and low-polarity electrolyte (0.2 M lithium perfluoroalkoxyaluminate (Li[Al(OR^F)$_4$]; R^F = C(CF$_3$)$_3$) in 1,2-difluoro-benzene). Cycling is sustained over 350 cycles with realistic conditions at a current density of 1 mA cm^{-2} and 48 μm thin Lithium-Metal-Anodes. This work provides a comprehensive understanding of how the artificial LiBFEP-SEI influences the performance of Lithium-Metal-Battery full cells, confirming the simplicity/effectiveness of the immersion process for the LiBFEP-coating.

1. Introduction

The mitigation of climate change requires major efforts, one of which is the electrification of the mobility/transport sector to reduce global greenhouse gas emissions.[1,2] Several countries have launched legislative initiatives to ban the sale of new internal combustion engines vehicles by 2035 or 2040, including the EU and other industrial countries.[3,4] Currently, Lithium-Ion-Batteries (LIBs) are used to power electrical vehicles. Due to the rapidly increasing demand for energy, in particular for the e-mobility segment, rechargeable batteries with higher energy content are urgently required. Among next generation high-energy-density rechargeable battery systems, Lithium-Metal-Batteries (LMBs) are a promising candidate. Due to lithium's high specific capacity (3860 mAh g^{-1}) and the lowest electrochemical potential of all metals (−3.04 V versus standard

S. Burger, J. Skrotzki, J. Büttner, W. Beichel, P. Klose, A. Fischer, I. Krossing
Institute for Inorganic and Analytical Chemistry
University of Freiburg
Albertstr. 21, 79104 Freiburg im Breisgau, Germany
E-mail: witali.beichel@ac.uni-freiburg.de; krossing@uni-freiburg.de
S. Burger, P. Klose, A. Fischer, I. Krossing
Freiburg Materials Research Center (FMF)
University of Freiburg
Stefan-Meier-Str. 21, 79104 Freiburg im Breisgau, Germany

The ORCID identification number(s) for the author(s) of this article can be found under https://doi.org/10.1002/aenm.202403195

J. Skrotzki, W. Beichel
Chair for Solar Energy Systems
Department of Sustainable Systems Engineering (INATECH)
University of Freiburg
Emmy-Noether-Strasse 2, 79110 Freiburg im Breisgau, Germany
J. Büttner, A. Fischer, I. Krossing
Cluster of Excellence livMatS
University of Freiburg
Georges-Köhler-Allee 105, D-79110 Freiburg, Germany
J. Büttner, A. Fischer, I. Krossing
Freiburg Center for Interactive Materials and Bioinspired Technologies (FIT)
University of Freiburg
Georges-Koehler-Allee 105, 79110 Freiburg im Breisgau, Germany
W. Beichel
High Performance Battery Technology GmbH
Schumannstr. 61, Bonn 53113
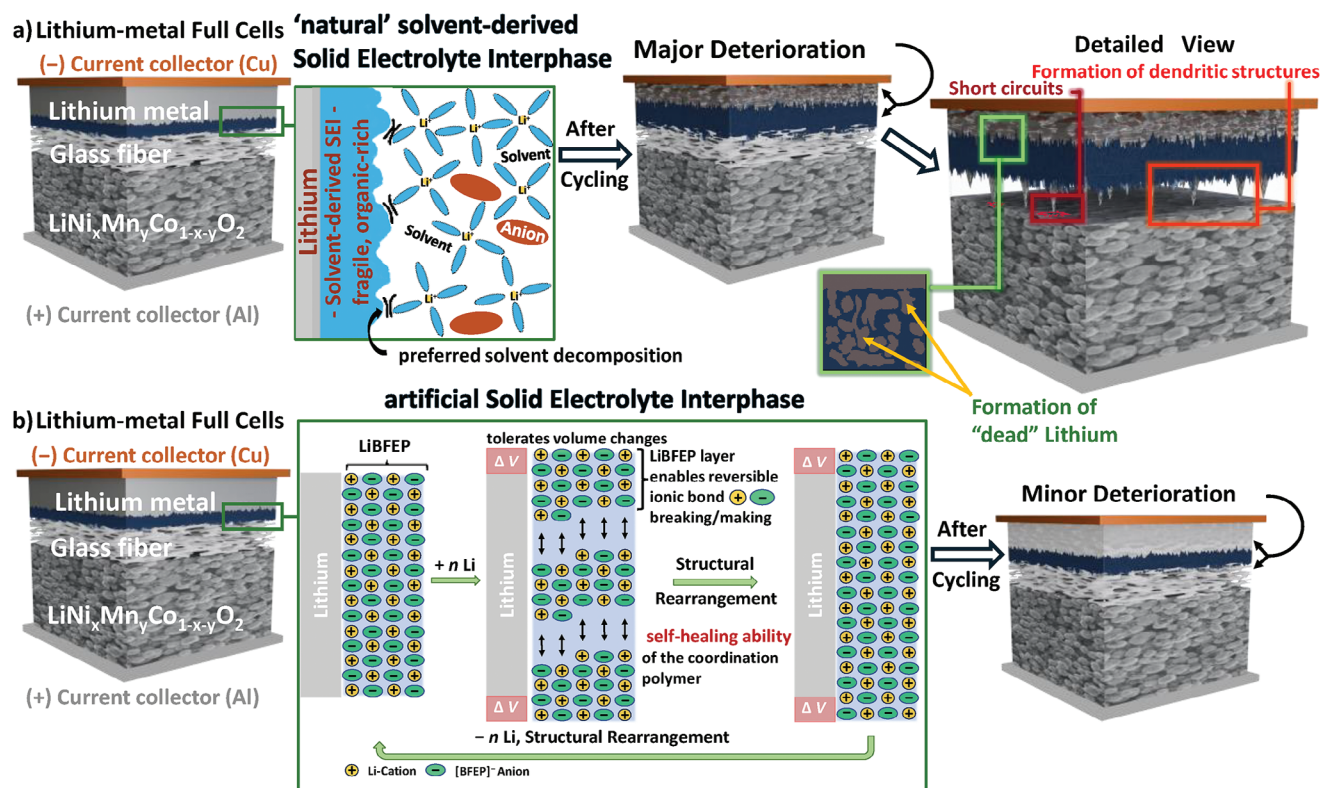
Figure 1. Influence of the SEI on the structural properties of LMAs in lithium-metal full cells after cycling. a) Presence of a "natural" solvent-derived SEI originates from the degradation of $LiPF_6$ solutions in carbonate mixtures. b) Application of an artificial LiBFEP-SEI with self-healing abilities.

hydrogen electrode), it includes the ideal prerequisites to satisfy the rapidly increasing demands for future mobility applications.[5–8] Hence, lithium-metal based anodes can boost the gravimetric energy density by at least 40% on cell level, since commercial LIBs using graphite-based anodes provide only a fraction (372 mAh g^{-1}) of the specific capacity compared to lithium metal.[8–10] However, although primary LMBs stem from the 1970s, a broader application of Lithium-Metal-Anodes (LMA) in rechargeable batteries failed due to challenges with the lithium metal-electrolyte interface/interphase.

1.1. LMA-Challenges

The high reactivity of lithium with liquid organic electrolytes in combination with the large volume expansion and shrinkage of lithium metal upon cycling leads to a depletion of the electrolyte with formation of an unstable solvent-derived solid electrolyte interphase (SEI).[11–13] With strongly solvating Li ions favoring ethylene carbonate (EC) in its primary solvation shell, the $[Li(EC)_x]^+$ ions are considered to be the main precursor of the SEI. The na-

tive plating/stripping behavior of lithium metal then leads to the generation of dendrites that pose a threat for catastrophic cell failure due to internal short circuits.[14,15] The LMA-volume change during cycling induces mechanical stress and the cracking of the SEI in comparison to standard graphite anodes.[16,17] The generated fresh Lithium surface exposed to the electrolyte leads to its fast consumption with continuous build-up of impedance by a thickening SEI. As a consequence, "dead" lithium forms, i.e., electrically insulated fragments of metallic lithium covered by a thick SEI.[18–21] Together, this leads to fast battery failure with high safety risks for the practical use of LMBs (**Figure 1a**).

1.2. Strategies to Mitigate LMA-Failure

Several strategies have been proposed to stabilize the lithium/electrolyte interface/interphase and reduce the parasitic reactions: ex situ generated artificial protective layers,[22–24] optimized electrolyte solutions with highly concentrated electrolytes (HCE), localized highly concentrated electrolytes (LHCE), and weakly solvating electrolytes (WSE).[25,26] These electrolyte systems generate anion-derived rather than solvent-derived SEIs, which seem to be beneficial for the presence of inorganic compounds such as lithium fluoride (LiF), lithium nitride (Li_3N), lithium oxide (Li_2O), and Lithium sulfide (Li_2S).[26,27] These compounds appear to stabilize a SEI due to their higher mechanical stiffness, larger bandgaps, and lower reduction reactivity.[28–32] Further approaches include micro/nanostructured anodes[21,33,34]

A. Welle
Institute of Functional Interfaces (IFG) and Karlsruhe Nano Micro Facility (KNMF)
Karlsruhe Institute of Technology (KIT)
Hermann-von-Helmholtz-Platz 1, 76344 Eggenstein-Leopoldshafen, Germany
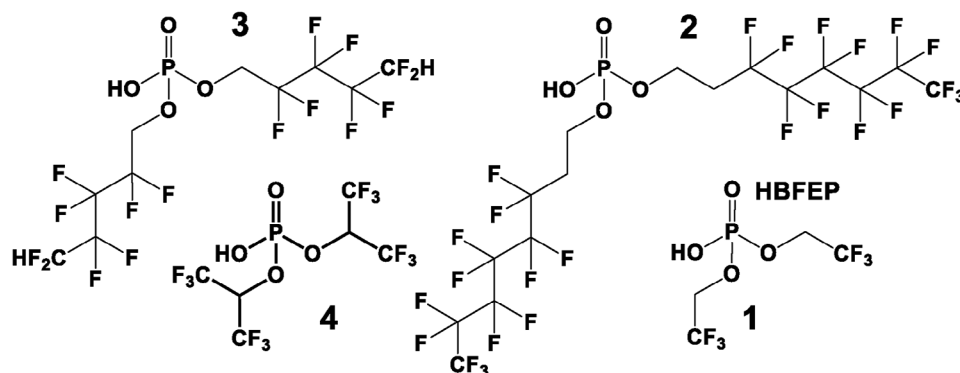
Figure 2. Overview of the compounds synthesized and used in this work.

and modified separator designs.[21,35,36] Their primary goal is to suppress dendrite growth. But, typically this increases inactive materials weight and reduces the energy density.[37–40] Yet, the concept of an ex situ generated artificial SEI is a promising strategy to enhance the performance of LMBs, since the (negative) influence of these additional layers on the overall energy density and the cell parameters is only small.[41]

1.3. Scope of this Work

Previously, we reported on the formation of an artificial SEI layer on LMAs by an inorganic coordination polymer based on a BFEP-backbone (bis(fluoroethyl)phosphate) that led to a significant increase in the cycle lifetime in Li-Li-symmetrical cells. This lifetime prolonging effect was attributed to the self-healing ability of the artificial SEI layer formed by LiBFEP. Hence, ionic bonds within the coordination polymer can reversibly break and reform during the Li-volume expansion upon cycling, since the protective layer adapts to the charge state and self-heals on the active Li metal. In contrast to this ionic coordination polymer, a classical polymer is held together by covalent bonds that cleave homolytically upon Li-volume expansion. In this case, very reactive organic radicals form leading to uncontrollable follow-up chemistry. Upon volume changes of the Li layer, the cation–anion distance within the coordination polymer might be increasing, but since the underlying ions are stable entities, the return to a new stable (healed) state as in Figure 1b is possible. In addition, the Li-ion conducting abilities of the coordination polymer were attributed to Li_2O_2 rhomboids that form as central structural moieties in the coordination polymer (further details see Section S1, Supporting Information).

Hitherto, this coating was tested only with an ether-based model electrolyte in symmetric Li-Li cells in combination with thick Li-metal electrodes (450 µm) and a corresponding large excess of lithium.[42,43] Here, this concept was applied toward realistic and long-lived rechargeable LMBs using a commercial carbonate-based standard electrolyte and $LiNi_xCo_yMn_{1-x-y}O_2$ (NMCs) cathode active materials (CAMs). Furthermore, several new fluoroalkyl phosphoric acids were synthesized and evaluated in Li-Li-symmetrical cells. For cycling to closely match a "real-world" battery, the following parameters were adjusted: i) reduced lithium inventory (Li-foil-thickness reduction from 450 µm

down to 48 µm), ii) reduced electrolyte amount (100 µL down to 55 µL), iii) increased loading of CAM (loading ≥ 1.0 mAh cm^{-2}), and iv) increased current density (from 0.1 mA cm^{-2} up to ≈1.0 mA cm^{-2}). The performance of the cells was investigated in situ and post-mortem to understand the function of the LiBFEP-based SEI. Furthermore, the LiBFEP-based SEI was also evaluated using the novel low-concentration and low-polarity electrolyte 0.2 M lithium perfluoroalkoxyaluminate (Li[Al(OR^F)$_4$]; R^F = C(CF$_3$)$_3$) in 1,2-difluorobenzene. In addition, the high-voltage cathode-protecting properties of LiBFEP proven for LNMO[44] were extended in this work to nickel-rich NMCs.

2. Results and Discussion

2.1. Synthesis HBFEP and Alternative Structures

To evaluate several fluoroalkyl phosphoric acids as artificial SEI-builders, the compounds displayed in **Figure 2** were synthesized. Note that the fluoroalkyl chain of **3** has a terminal -CF$_2$H group, replacing the -CF$_3$ group in compounds **1** and **2**. The CF$_2$H-group is reported to exhibit more facile chemical degradability, improving its biocompatibility favorable in the context of ongoing PFAS-discussions.[45]

The synthesis of the phosphoric acid derivate HO(O)P(OCH$_2$CF$_3$)$_2$ (HBFEP) **1** was published by our group[43] by conversion of CF$_3$CH$_2$OH with P$_4$O$_{10}$ in a ratio of 8:1. The acid was obtained as a crystalline, colorless solid in 33% yield on a multigram scale. Here, we use a slightly modified water-based route following Mahmood et al. according to Equation (1),[46] in which the commercially available fluorinated triester tris(2,2,2-trifluoroethyl)phosphate (R^F = -CH$_2$CF$_3$) was stirred with water at 48 °C for 72 h.[46]

$$O = P(OR^F)_3 + H_2O \rightarrow HO(O)P(OR^F)_2 + HOR^F \tag{1}$$
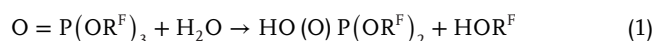
Product **1** was obtained in 47% yield. Similarly, the synthesis of **3** was conducted in 61% yield via Equation (1) with the triester P(OR^F)$_3$ and R^F = -CH$_2$(CF$_2$)$_3$CF$_2$H. The only relevant side products were (HO)$_2$P(O)(OR^F) (5%) and nonconverted triester (23%).[46] Two polyfluoroalkyl phosphoric acid diesters were synthesized similarly to the original procedure for compound **1**. Hence, using R^F-OH with R^F = -CH$_2$CH$_2$-(CF$_2$)$_5$CF$_3$ in Equation (2) gave after multiple recrystallizations compound **2** in 8%

2403195 (3 of 21)

**ADVANCED
SCIENCE NEWS**

www.advancedsciencenews.com

**ADVANCED
ENERGY
MATERIALS**

www.advenergymat.de

Table 1. Overview of the different coating conditions used and their abbreviations.

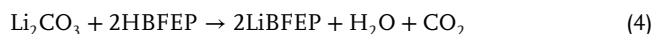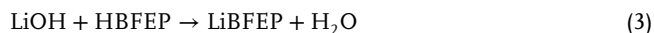| Coating procedure	Used materials	Abbreviation
#1	Lithium foil (48 µm) treated with 0.05 M HBFEP solution in DME for 4 min.	LF005H4
#2	Lithium foil (48 µm) treated with 0.05 M solution of the polyfluoroalkyl phosphoric acid diesters 2–4 in DME for 4 min.	LF005HA4
#3	Commercial nickel-rich NMC850510-sheet treated with 0.7×10^{-3} M HBFEP solution in DME for 30 min and drying for 1 h in the vacuum chamber.	NMC07mH30
#4	Lithium coins (450 µm) treated with 0.05 M HBFEP solution in DME for 4 min.	LC005H4
#5	Lithium coins (450 µm) treated with 0.05 M HBFEP solution in DME for 4 min and washed with pentane for 15 min before acid treatment.	LC005H4P
#6	Lithium foil (48 µm) was treated with 0.05 M $HNTf_2$ solution in DME for 1 min.	LF005HN1

yield with 80% purity and with 20% of $(HO)_2P(O)(OR^F)$ as only side product.[43]

$$8HOR^F + P_4O_{10} \rightarrow 4HO(O)P(OR^F)_2 \qquad (2)$$
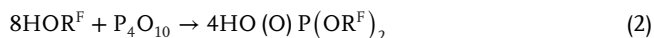
With the long fluoroalkyl chains, lower solubilities of the Li-salts of **2** and **3** and changes at the electrode/electrolyte interface/interphase were expected, if compared to **1**. To study the influence of branching versus linear chains on the coating on Li metal, pure $HO(O)P[OCH(CF_3)_2]$ (HFiP) **4** with branched hexafluoroisopropyl-residue was synthesized according to route (2) in a poor yield of 4.2%.[43]

2.2. Coating of 1–4 onto Li-Coins (450 µm) and Li-Foil (48 µm) by a Simple Immersion Process

The phosphoric acid derivates **1–4** may react with basic surface species like Li_2CO_3 and Li_2O present on the Li-metal-surface but also on the surface of the Ni-rich CAMs according to Equations (3) and (4), exemplarily formulated for HBFEP.
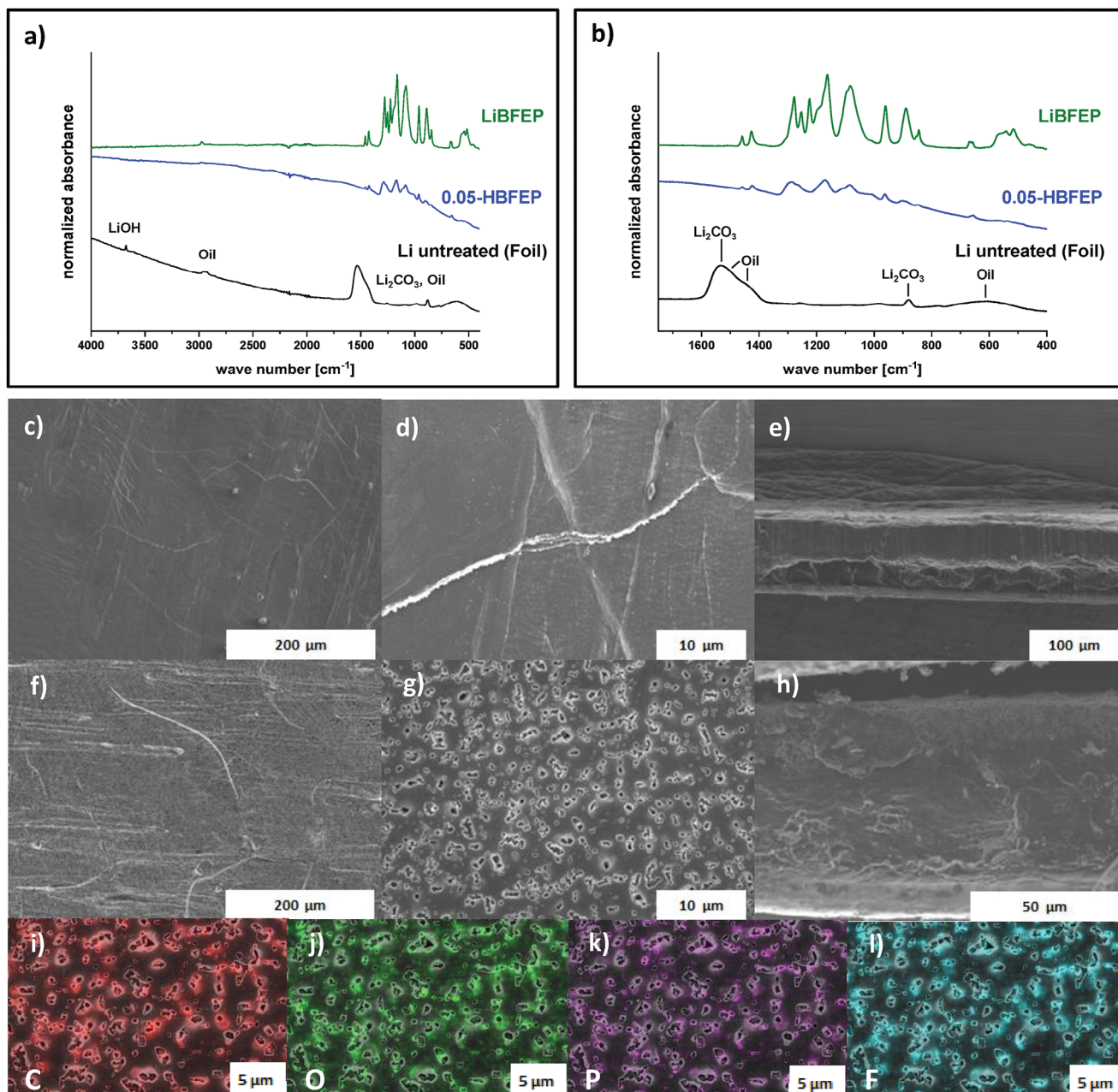
$$LiOH + HBFEP \rightarrow LiBFEP + H_2O \qquad (3)$$

$$Li_2CO_3 + 2HBFEP \rightarrow 2LiBFEP + H_2O + CO_2 \qquad (4)$$

$$Li^0 + HBFEP \rightarrow LiBFEP + 0.5H_2 \qquad (5)$$

Thus, **1–4** were applied on Li metal by a simple immersion process. The Li-metal foils or discs were stirred in a 0.05 M solution of the diesters **1–4** in 1,2-dimethoxyethane (DME) for 4 min (**LF005HA4**, see **Table 1**).[42] Afterwards, the solution was removed and the LMAs were dried inside a glovebox. Since gas evolution was only very minimal, the redox reaction according to Equation (5), kinetically hindered compared to the acid–base reactions (3) and (4), is expected to play only a small role. Addi-

tional tests to apply HBFEP on Li metal in dip-coating and spin-coating processes (see Section S2, Supporting Information), were inferior to the immersion process. Hence, the immersion process was selected for **1–4**.[47] All coating conditions used (LMA and also NMC cathodes) including the alternative acid $HNTf_2$ (Tf = SO_2CF_3) used for evaluation purposes, are listed/described in Table 1 with the nomenclature used hereafter.

2.3. Coating Characterization: From 450 µm Thick Li-Metal Coins to 48 µm Thin Li-Metal Foils

Our previous work used 450 µm thick LMAs in combination with a model electrolyte known to rapidly degrade the anode, i.e., 1 M Li[OTf] solution in TEGDME (tetraethylene glycol dimethyl ether; OTf = OSO_2CF_3).[42] Yet, such thick LMAs have a theoretical areal capacity of 92.8 mAh cm^{-2} that is about 20 times higher than the one in commercial cathodes of 3–5 mAh cm^{-2}.[46,48,49] Hence, thick LMAs represent a quasi-infinite lithium reservoir that drastically reduces the specific energy on the cell level, as does the amount of electrolyte. The latter and the cathode loading also influence the cycling performance. Hitherto, still relatively few LMB reports take all these parameters into account and would, therefore, result in specific energies far below 100 Wh kg^{-1}.[40,50,51] To achieve specific energies beyond 300 Wh kg^{-1}, the Li-amount/the Li-thickness of LMAs has to be low. Hence, **Figure 3** shows the characterization and the morphology of the 48 µm thin Li-foil (9.9 mAh cm^{-2}) used in this work. The Attenuated Total Reflectance Infrared (ATR-IR) spectra confirmed the presence of paraffine and silicon oil on the surface of the untreated lithium electrodes, also observed with Time-of-Flight Secondary Ion Mass Spectrometry (ToF-SIMS) measurements (Figure S15, Supporting Information). Figure 3a,b shows the characteristic LiBFEP-modes between 1500 and 850 cm^{-1} on the 0.05-HBFEP treated Li-foil.[42] Although SEM images of the 0.05-HBFEP treated Li-foil (**LF005H4**, see Table 1) show at first glance a similar morphology to the untreated Li-foil (Figure 3c,f), magnification reveals a porous structure with crater-like holes in the order of several micrometers (Figure 3f–h). Scanning Electron Microscopy-Energy Dispersive X-ray Spectroscopy (SEM-EDX)-Mappings (Figure 3i–l) indicate a complete coverage of the Li surface of the 0.05-HBFEP treated Li-foil with C, O, P, and F, proving the presence of LiBFEP, similar to thick LMAs.[42] Higher BFEP-intensities evolve at the edges of the crater-like holes, possibly related to an enhanced reaction of the basic surface species, e.g., Li_2CO_3, Li_2O, or metallic Li itself with the HBFEP-coating solution. Alternatively, the crater-like hole morphology[42] might result from the expulsion of LiBFEP crystallites in the SEM vacuum chamber upon evacuation and vaporization of underlying solvent residues.

The cross-section images (**Figure 4a**) of the 0.05 M HBFEP-treated Li-foil agree with a porous layer of almost 10 µm thickness, which reaches into the Li-bulk. The thickness of this layer indicates an interaction of the HBFEP acid with the basic surface layer and also, to some extent, with metallic Li. Within the porous layer, EDX-mapping analyses (Figure 4b–e) show higher signal intensities of the elements C, O, P, and F and—likely an artifact introduced by cutting the electrodes—also lower intensities in deeper areas of the Li-bulk that were dragged

**ADVANCED
SCIENCE NEWS**

www.advancedsciencenews.com

**ADVANCED
ENERGY
MATERIALS**

www.advenergymat.de

Figure 3. a,b) ATR-IR spectra of HBFEP-treated Li-foil in comparison to reference spectra of untreated Li-foil and powdered LiBFEP. c,d) SEM top view images of the surface of the used Li-foil and e) its cross-section. f,g) SEM top view images of the surface of 0.05-HBFEP treated Li-foil and h) its cross-section. i,j) EDX-Mapping analysis of the surface of a 0.05-HBFEP sample and the corresponding elemental distribution of C (red), O (green), P (purple), and F (blue).

from the top layer across the cross-section. The presence of C, O, P, and F supports the formation of a LiBFEP-rich porous layer.

To determine the concentration of HBFEP in the coating solution before and after the immersion process, Nuclear Magnetic Resonance (NMR) spectroscopic measurements were conducted against an *o*-difluorobenzene internal standard. Here, a consumption of one-tenth of the amount of HBFEP in the coating solution was found. Normalization to the geometric surface area of the used Li-metal foil results in an area loading of

0.945 mg cm^{-2} of the LiBFEP formed on the Li-metal electrodes. Assuming a flat crystalline layer, this loading would correspond to a thickness of about 5.5 µm (using the known[42] crystal density of (LiBFEP)$_2$·DME of $\rho_{x-ray} = 1.726$ g cm^{-3}; cf. Section S3, Supporting Information). Given the visible porous structure of 10 µm thickness, approximately 40% of the total layer content may be attributed to pores and 60% to solid LiBFEP material. Application of high vacuum during the SEM measurements will likely increase the visible layer thickness by evaporation of included solvent molecules. Hence, the "true" porosity within the
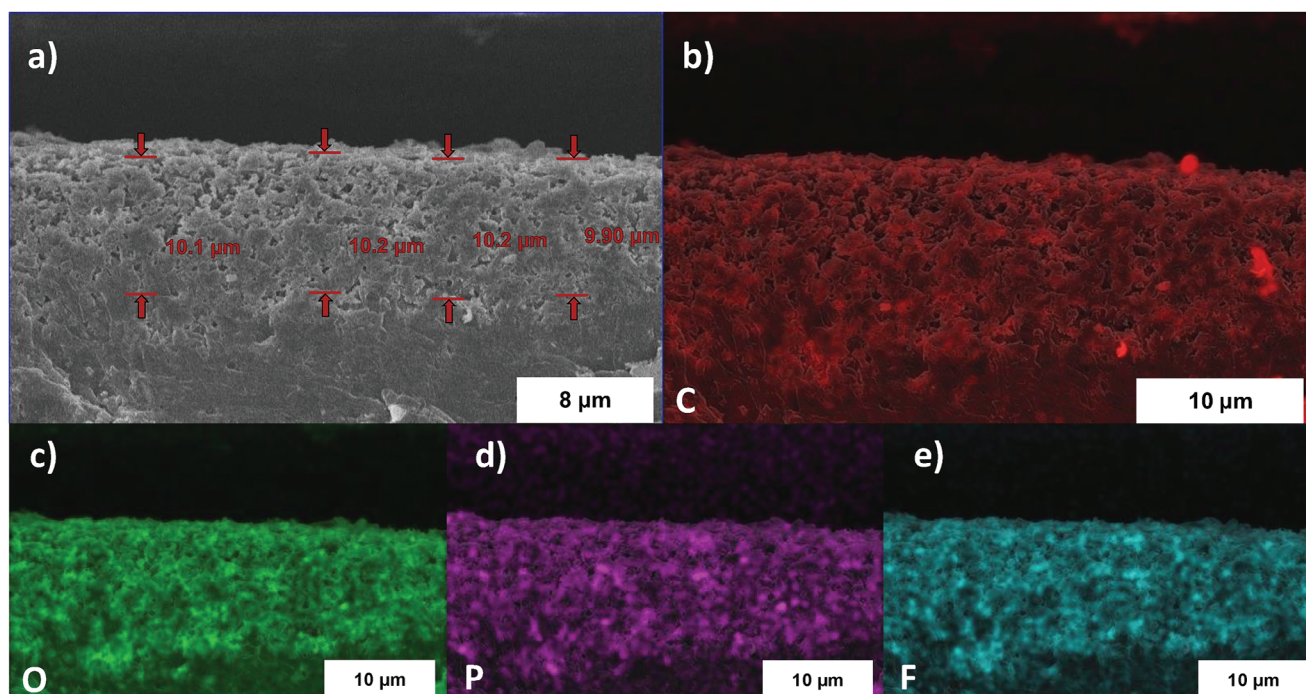
Figure 4. a) SEM cross-section of the 0.05 м HBFEP treated Li-foil. b–e) EDX-Mapping analysis of the 0.05-HBFEP treated Li-foil and the corresponding elemental distribution of C (red), O (green), P (purple), and F (blue).

battery system should neither reach an extent visible in the SEM nor influence the performance of HBFEP-treated Li anodes negatively.
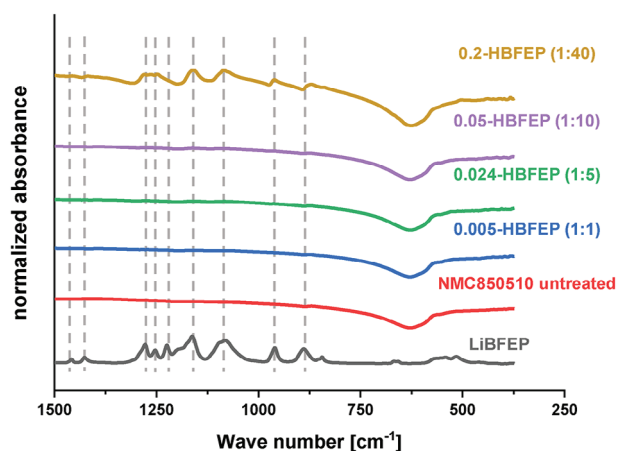
An analogous procedure was used to coat **2–4** from a 0.05 м DME solution to the thin lithium foil (Table 1, Section 2.2). Corresponding cycling data of Li-Li symmetrical cells are shown in Section 3.1.

2.4. Coating of Nickel-Rich NMC850510 Cathode Sheets with HBFEP

Nickel-rich $LiNi_xCo_yMn_{1-x-y}O_2$ (NMCs) are promising CAM for high-performance battery electric vehicles (BEV) due to their high specific capacities that exceed > 215 mAh g^{-1} in the nickel-rich version NMC850510.[52] However, there are several problems, which hinder their broader implementation into the market. Apart from electrolyte degradation, Li/Ni cation mixing and cracking of the secondary particles during cycling, especially the nickel-rich NMCs are prone to the surface formation of Li_2CO_3 and LiOH upon exposure to CO_2 and moisture (H_2O).[53,54] In addition, their synthesis requires an excess of lithium with the consequence that residual lithium often remains at the surface.[55,56] The residual surface lithium compounds lead to degradation of electrolyte components and the formation of an insulating passivation layer during operation, which impedes lithium diffusion and significantly increases the charge-transfer resistance during cycling.[54,55] Also, the powder pH value of the CAM increases due to the very Bronsted-basic LiOH and Li_2CO_3 residues on the surface of the CAM particles and can cause gelation of the electrode slurry.[55]

One remedy to this may be the application of HBFEP on nickel-rich NMCs to remove the Bronsted-basic surface layer according to Equations 3 and 4. Moreover, the concomitant formation of a thin layer of LiBFEP could result in the protection of the CAM particle surface,[44] similar to the use of LiBFEP as electrolyte additive (0.1...0.5 wt%) for high voltage full cells with LNMO cathode ($LiNi_{0.5}Mn_{1.5}O_4$) and cutoff voltages around 4.8 V. Hence, a commercial-grade nickel-rich NMC850510-sheet was treated similarly to the coating of Li metal and was placed in a 0.7×10^{-3} м solution of HBFEP in DME for 30 min (**NMC07mH30**, see Table 1). The concentration was set lower to 0.7×10^{-3} м, to exclude a Li$^+$/H$^+$ exchange with the acid HBFEP in the CAM matrix, as observed with water-based electrode pastes for Ni-rich electrode materials.[57,58] In addition, several reports indicate superior performances of coating processes by treatment at low concentrations.[59,60] **Figure 5** shows the ATR-IR spectra of the commercial-grade NMC850510-sheet after treatment with different HBFEP solutions. The IR-signature of LiBFEP—similar to the one observed on the Li-foil—becomes visible at concentrations above 0.2 м HBFEP in DME and demonstrates the successful immersion coating principle (Figure 3, Figure S2a, Supporting Information).

The ratios in parentheses in Figure 5 represent the amount of HBFEP present with respect to the measured 0.94 wt% shares of LiOH and Li_2CO_3 in the pure NMC850510 powder as determined by titration. This amount was used as a reference to adjust the HBFEP-concentration in solution and also for the coating of the commercial NMC-sheet (entire spectrum Figure S4, Supporting Information). However, due to the strong absorbance of NMC850510 and the composite environment of the commercial NMC-sheets, the IR-intensities of the LiBFEP-surface on the

**ADVANCED
SCIENCE NEWS**

www.advancedsciencenews.com

**ADVANCED
ENERGY
MATERIALS**

www.advenergymat.de

Figure 5. Magnified ATR-IR spectra of a commercial NMC850510-sheet after treatment with HBFEP solutions 0.005–0.2 M between 250 and 1500 cm^{-1} with marked bands of LiBFEP. The ratios given in parentheses correspond to the ratio of titration-determined base content (LiOH, Li$_2$CO$_3$) in pure NMC850510 powder and the concentration of HBFEP in the coating solution.

coated NMC-sheet are very weak, especially at low concentrations of the coating solution. Hence, NMR spectra were recorded to compare the concentration of HBFEP in the solution before and after the coating step, similar to the coating of the Li-metal foil. From the decrease of the HBFEP-concentration of 1.2 mmol with respect to the concentration before the coating step and normalization to the area of the immersed NMC-sheet, an area loading of LiBFEP of 0.494 mg cm^{-2} on the NMC-sheet was determined. This loading would correspond to a thickness of 3 μm for a flat crystalline layer, calculated as in Section 2.3.[42] Next, the modified NMC850510-electrode sheets were investigated by electron microscopy. **Figure 6** shows the NMC electrode from different angles. The surface of the NMC electrodes consists of spheroidal particles of around 10 μm size (Figure 6a,b). The cross-section (Figure 6c) discloses a homogeneous, about 50 μm thick cathode composite on the aluminum substrate. The uniform distribution of the Nickel signal intensity along the NMC-particles and the overlapping signal intensity for phosphorus agree with the morphology of the CAM particles and indicate a homogenous coverage with LiBFEP (EDX-mapping, Figure 6d–g top view, h-k cross-section; also Figure S5c, Supporting Information). For a comment on shadowing effects see Section S5 (Supporting Information).

3. Electrochemical Cycling in Symmetrical, Half, and Full Cells

3.1. Electrochemical Tests of Coated Electrodes in Symmetrical Cells

HBFEP-treated lithium electrodes in Li-Li symmetrical cells showed a 3.6-fold lifetime extension using a model electrolyte with thick Li-metal anodes (Figure S8a–c, Supporting Information).[42] This electrolyte (1 M LiOTf in TEGDME) was used to visualize the life-prolonging effect of LiBFEP-coating resulting from its limited transport properties and its insta-

bility against lithium,[61,62] but requested low current densities of 0.1 mA cm^{-2}/areal capacities of 0.1 mAh cm^{-2} to demonstrate the effect of LiBFEP-coating in Li-Li symmetrical cells. Here, we performed more realistic electrochemical measurements with the commercial carbonate-based electrolyte LP57 (1 M LiPF$_6$ in ethylene carbonate (EC)/ethylmethyl carbonate (EMC) 3:7 wt%) at increased current density/areal capacity of 1.0 mA cm^{-2}/1.0 mAh cm^{-2} (= 1C rates).[63]
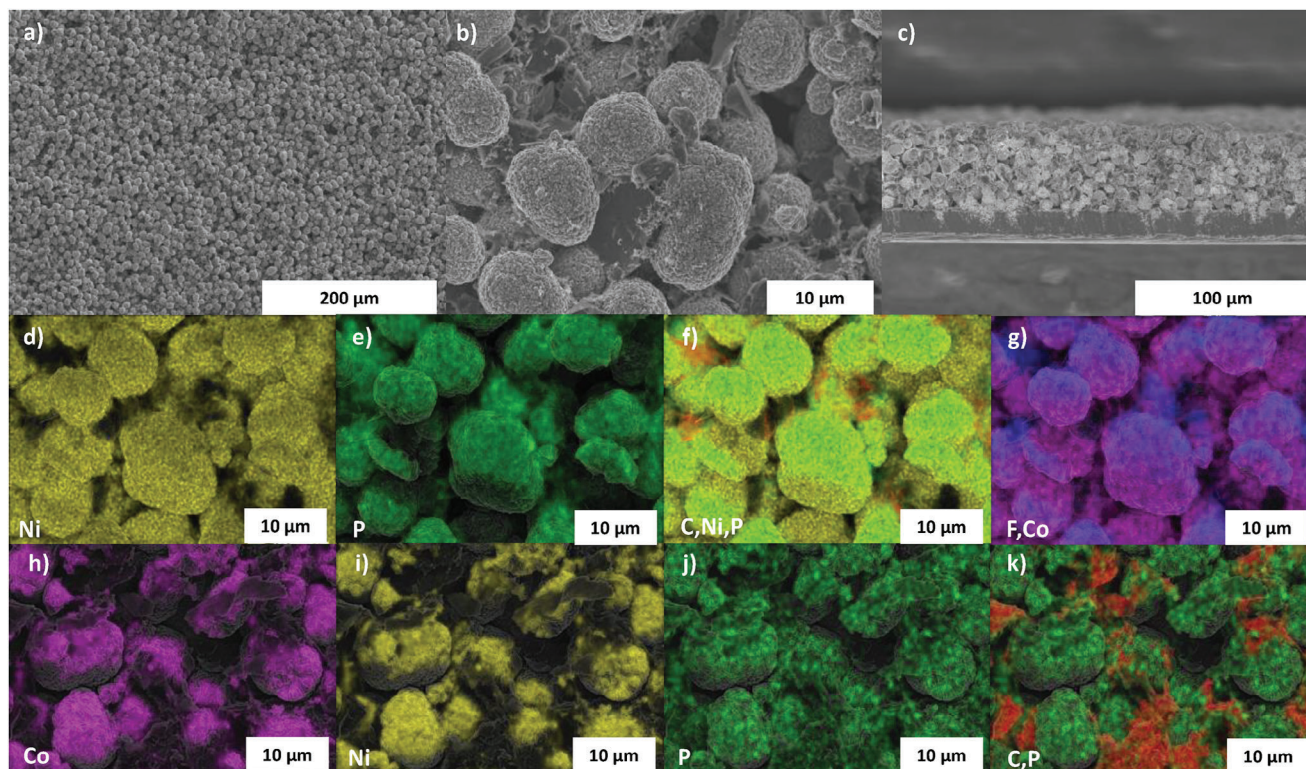
3.1.1. Thick Li Coins

For comparison, also thick Li-coins were measured. Here, the lifetime prolonging effect after their immersion (protocol **LC005H4**, Table 1) is small (+26%, Figure S7a–c, Supporting Information), possibly resulting from the 10-fold increase in the current density and other effects (see Section S6, Supporting Information, for discussion).

3.1.2. Thin Li-Foil

To minimize the influence of the thickness of the Li electrodes and to prevent the masking of degradation processes caused by excessive lithium consumption, Li-Li symmetrical cells with a thin Li foil (48 μm) on Cu (12 μm) were built. Cycling data in **Figure 7** indicate an accelerated electrolyte degradation, consumption of the Li inventory, and formation of a porous interphase of dead Li for the pristine Li electrodes with an average lifetime of 21 cycles until reaching the ±3 V potential limit. By contrast, HBFEP-treated cells (**LF005H4**, Table 1) survive on average 39 cycles. High overpotentials of ±341 mV for the cells with pristine Li electrodes are visible upon zooming to the V(t)-Diagram between the 1st and 5th cycle (Figure 7b), particularly in the first charging step. 0.05-HBFEP cells display a much lower overpotential of only ±59 mV in the same area and even after 19 cycles (±41 mV; Figure 7c). At this time, the pristine cells are already eight times higher at ±338 mV and shortly after the overpotential increases exponentially, indicating cell death. Beneficially, the lifetime of the 0.05-HBFEP cells is almost doubled (+86%). Increasing overpotentials typically arise from hindered Li plating/stripping processes occurring at the SEI formed by chemical reaction upon contact of state-of-the-art electrolytes with the Li-metal anode.[26,62,64] This initial SEI reduces Li-ion conduction, induces high overpotentials, presents a kinetic barrier for plating and stripping of Li ions in cells with pristine Li electrodes, and leads to irregular and sharp voltage profiles. By contrast, the 0.05-HBFEP cells run with low overpotentials and flat voltage profiles, indicating a superior Li platting/stripping behavior on the LMA-surface.

Hence, the artificial Li-ion conducting LiBFEP-SEI induces low and stable overpotentials over a wide cycle range. Apparently and contrary to the pristine cells, the coating reduces the formation of dead Li and allows for good mass transport through the porous interphase.[19,21] Yet, the absolute number of cycles achieved with LP57 is lower than that with the LiOTf model electrolyte (Figure S8a–c, Supporting Information) at low current density (0.1 mA cm^{-2}). However, with the reduced Li content in the foil (48 μm versus 450 μm coin) and the 10-fold increased

**ADVANCED
SCIENCE NEWS**

www.advancedsciencenews.com

**ADVANCED
ENERGY
MATERIALS**

www.advenergymat.de

Figure 6. a,b) SEM top-view of a commercial-grade NMC850510 electrode. c) SEM cross-section of a commercial-grade; NM850510-sheet. d–g) EDX-Mapping analysis with 18 kV (top-view) of a HBFEP-treated NMC-sheet and the corresponding elemental distribution of C (red), F (blue), P (green), Ni (yellow) and Co (purple). h–k) EDX-Mapping analysis with 5 kV (cross-section) of a HBFEP-treated NMC-sheet and the corresponding elemental distribution of C (red), P (green), Ni (yellow), and Co (purple).

current density (0.1 mA cm^{-2} versus 1.0 mA cm^{-2}) plus a 10-fold increased areal capacity (0.1 mAh cm^{-2} versus 1.0 mAh cm^{-2}), the reduction of the lifetime is logical.[40,50] Overall, the life-prolonging effect of the HBFEP treatment reaches 86% for the thin Li foil electrodes and is significantly higher than for the thick LMAs (Figure S7a–c, Supporting Information, 26%). It appears that the from 100 µL (model electrolyte) to 60 µL (LP57) reduced amount of electrolyte dissolves less LiBFEP from the electrode surface. Hence, the positive effect of the LiBFEP-coating is even more pronounced.

3.1.3. Testing of 2–4

LiBFEP is slightly soluble in DME and carbonate-based electrolytes. Thus, the diesters **2** and **3** were chosen as alternatives to HBFEP with significantly longer side chains and potentially reduced solubility in nonfluorinated solvents such as DME or organic carbonates. Their steric demand could also generate novel structures of the coordination polymer inducing flexibility and/or Li-ion conductivity. Furthermore, compound **4** exhibits a second acidic (C-)H proton that could react with lithium (compounds)
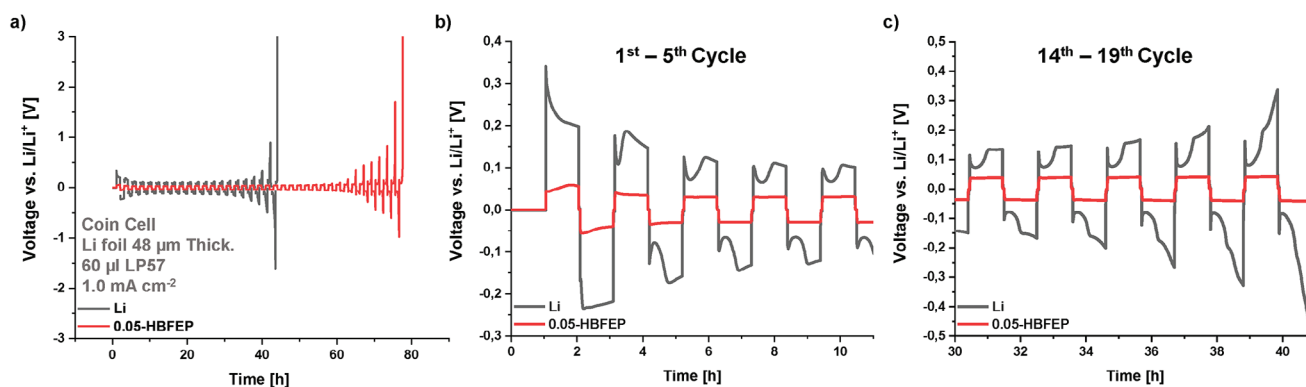
Figure 7. a) Overall course of Li-Li symmetrical cells at 1 mA cm^{-2} in LP57 (25 °C) containing thin Li-metal anodes; b,c) magnified regions of a) demonstrating the evolution of the investigated cells. Quadruplicates were built for each series of cells.

**ADVANCED
SCIENCE NEWS**

www.advancedsciencenews.com

**ADVANCED
ENERGY
MATERIALS**

www.advenergymat.de
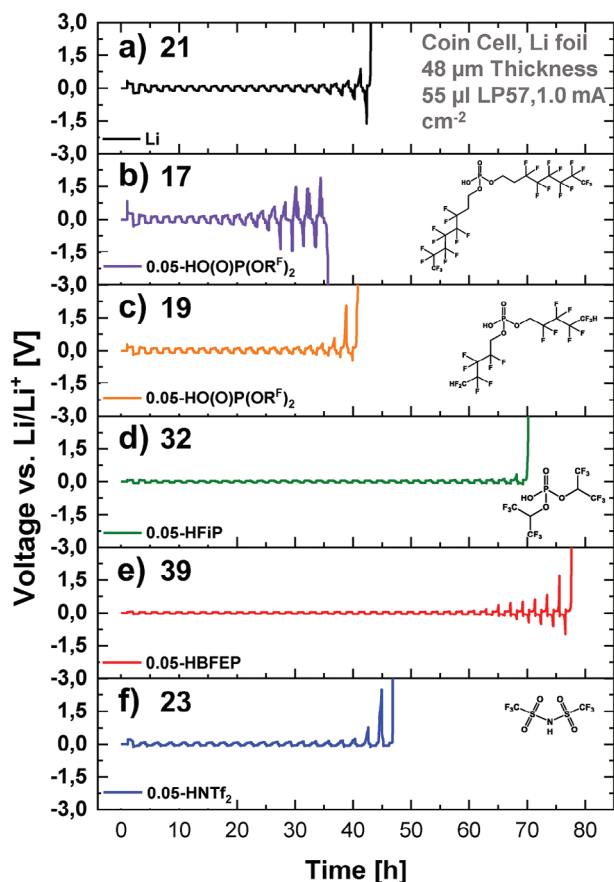
Figure 8. A representative set of performances of Li-Li symmetrical cells at 1 mA cm^{-2} in LP57 and coated with different phosphoric acids diesters 1–4 in comparison to; a) pristine Li anodes; diesters $HO(O)P(OR^F)_2$; b) R^F = -$CH_2CH_2(CF_2)_5CF_3$; c) R^F = -$CH_2(CF_2)_3CF_2H$); d) HFiP; e) HBFEP, and f) $HNTf_2$ at 25 °C. The numbers displayed in the figure represent the number of cycles until the cutoff voltage of 3 V was reached. Quadruplicates were built for each series of cells.

at the C2 position and induce formation of a cross-linkage between different coordination polymer chains. For compound **3**, literature precedence stresses that a terminal CF_2H group could enable a pathway for chemical degradation, possibly opening a starting point for biodegradability. Under the current PFAS discussions, this is gaining increased attention.[45,65] Similarly to **1**, **2–4** were tested in Li-Li symmetrical cells built from thin Li foil and all coatings were applied analogously to protocol **LF005HA4** (Table 1). **Figure 8** shows an overview of the cycling tests in Li-Li symmetrical cells, with the numbers displayed with the cycling test corresponding to the cycle number when the cutoff voltage of 3 V was reached. Diesters **2** and **3** did not lead to any improvement (Figure 8b,c) and the lifetime is even shorter in cells treated with diester **2** than in those with untreated Li electrodes. For **2**, the irregular voltage profiles and rapidly increasing overpotentials in Figure 8b indicate nonuniform Li-plating and stripping. Only Li-Li symmetrical cells treated with the HFiP-diester **4** (Figure 8d) show by 52% to 32 cycles increased lifetime of the cells. Profiles of the charging and discharging steps are flat and substantially lower than those shown in Figure 8b,c. Yet, a similar prolongation

of the lifetime as with HBFEP treatment was realized by none of the other diesters.

3.1.4. Surface Cleaning with $HNTf_2$

From the preceding, one could argue that the beneficial performance of the artificial LiBFEP layer could result from the simple removal of the basic surface species such as LiOH and Li_2CO_3 by the acid–base HBFEP-treatment and not from the formation of the LiBFEP layer itself. Since bis(trifluoromethane)sulfonimide ($HNTf_2$) is a strong acid, a related treatment should similarly lead to the removal of the basic surface layer. Hence, $HNTf_2$ was also used for coating LMAs (Figure 8f, **LF005HN1**, see Table 1). But, in contrast to LiBFEP, the $LiNTf_2$ formed upon reaction is well soluble in the coating solution and does not remain on the surface. Cells treated with $HNTf_2$ in Figure 8 show almost no improvement of their lifetime.[66,67] This indicates that the life-prolonging effect of the HBFEP treatment does not originate from the simple removal of the basic surface layer from Li.

Overall, the effects of the treatment of the Li electrodes with the phosphoric acid diesters in a solution chemical process are a compromise between several factors: Acid strength, steric effects, the coating time, and the concentration of the coating solution might play an important role. According to Figure 8, HBFEP seems to give the best combination. However, the different diesters may require other application conditions, but to restrict the scope, only HBFEP was selected to further study the influence of such an artificial SEI on LMAs in realistic LMB full cells in Section 3.3.

3.2. Electrochemical Tests of Coated NMC850510 Electrodes in Half Cells

To evaluate the influence of the LiBFEP-coating on nickel-rich NMC850510 cathodes, electrochemical tests in half cells were conducted with pristine and 0.7×10^{-3} M HBFEP-treated cathodes (**NMC07mH30**, see Table 1). The NMC850510 cathodes were dried after the HBFEP treatment for half an hour under dynamic vacuum in the vacuum chamber of the glovebox (<1 mbar) to remove the volatiles from the HBFEP treatment (cf. Equation 3 and 4). The half cells were cycled at 0.5 C-rate to keep the influence of the pristine lithium counter electrode low. Half-cell cycling data shows over 250 cycles an improved performance of HBFEP-treated cells (**Figure 9**a) with reduced standard deviations (area marked in faint red) compared to cells without HBFEP treatment (area marked in faint gray). HBFEP-treatment increases the cycling-reproducibility from the very beginning and improves average charging and discharging voltages (Figure 9b).

3.2.1. CC and CV Share of the Charging

The cycling of the half cells was performed with a constant current and constant voltage (CC-CV) charging protocol. Here, the share of the constant current capacity (CCC) and the constant voltage capacity (CVC) gives an insight into the conditions inside the cells,[68] similar to the constant current charging time
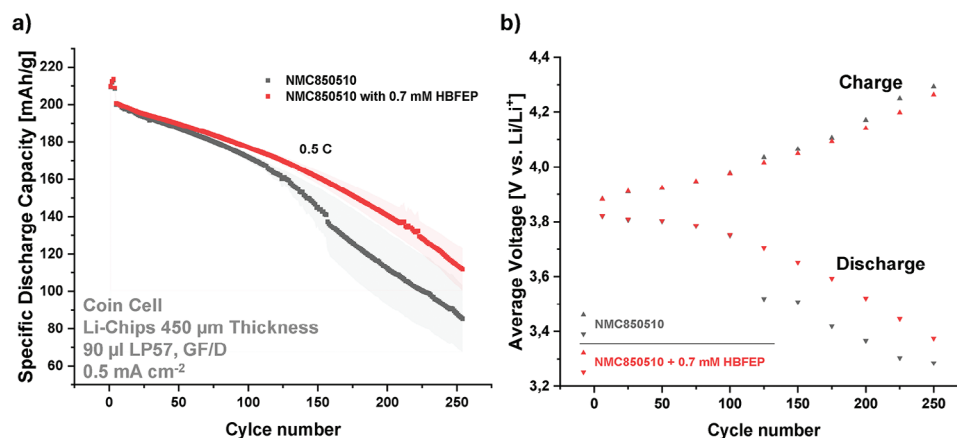
Figure 9. a) Cycling data of half cells (coin cells) HBFEP-treated NMC850510 cathodes in comparison with cells without HBFEP treatment. b) Development of the average voltage for the charge/discharge step of the half cells over the course of 250 cycles (without HBFEP/with HBFEP treatment) at 25 °C. Quadruplicates were tested for each series of cells.
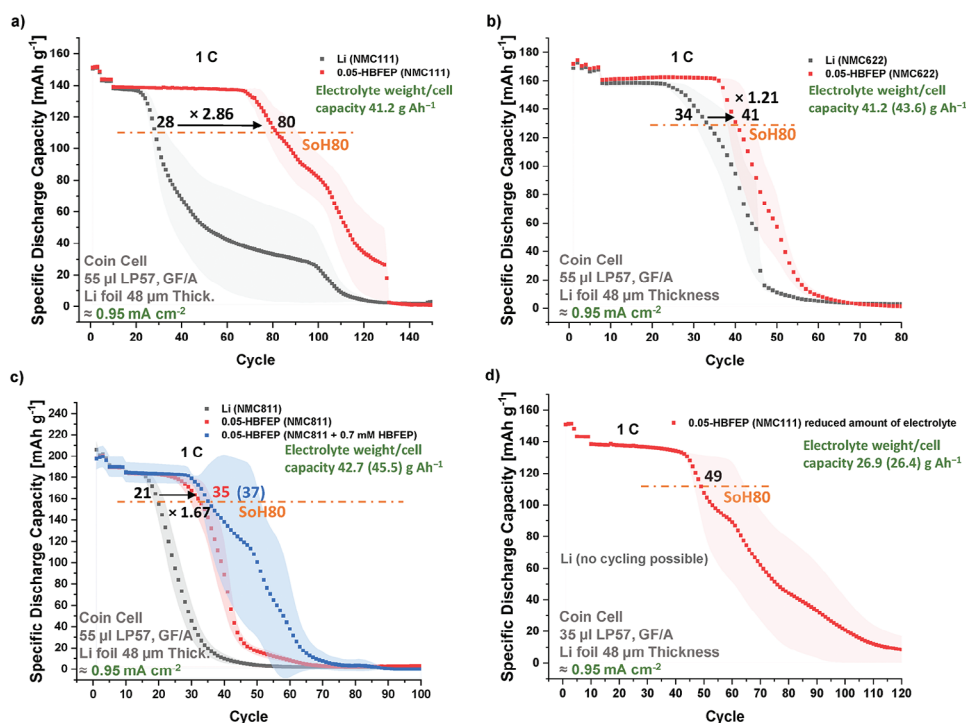
(CCCT) and the constant voltage charging time (CVCT).[69,70] The CVC should be as small as possible since the CV step takes much time, and the contribution to the charge capacity is limited. On the other hand, high CV shares indicate sluggish Li ion diffusivity in the CAMs and the presence of a concentration gradient of Li ions.[71,72] The extent of the increase in the CV share provides information on the stability and the dimension of undesired processes of the CAMs. The polarization of the cells and CVC capacities are collected in **Table 2**, with the cell polarization referenced to the average voltages at the 6th cycle, i.e., completion of cell formation. Figure S9 (Supporting Information) also shows the voltage profiles of the different cells during the cycling. For cells without the HBFEP treatment, a shift of the voltage profiles to higher values resulted so that the cutoff voltages are reached earlier and the (unfavorable) CVC share increases quicker.

The difference in the polarization becomes significant after 125 cycles mainly in the discharging step, resulting in a prolonged discharging for the HBFEP-treated cells as the cells do not reach the cutoff voltage, which improves the cycling performance of those cells.[68] HBFEP treatment enables utilization of 59.5% of the initial discharge capacity after 225 cycles, whereas with untreated NMC850510cathodes, only 48.7% are available. In addition, the CVC increase of cells with untreated cathodes accelerates with advanced cycling. The HBEFP-treatment delays the voltage shift during charging and discharging, especially at later cycling stages (≥200 cycles) when the differences between the voltage profiles of coated and pristine cells become more significant. Both observations indicate the beneficial effect of the LiBFEP-coating on the CAM–apparently resulting from (partial?) removal of the basic surface species from the NMC particles and suppression of electrolyte side reactions attributed to

Table 2. Overview of the polarization of the cells according to the average voltages (compared to 6th cycle) and the share of the CVC on the overall capacity.

Cycle	$\Delta V_{\text{average Voltage}}$ NMC850510[a]		$\Delta V_{\text{average Voltage}}$ NMC850510 + 0.7 HBFEP[a]		Share CVC NMC850510 [%]	Share CVC NMC850510 + 0.7 × 10^{-3} м HBFEP [%]
	Charge [mV]	Discharge [mv]	Charge [mV]	Discharge [mV]		
6	–	–	–	–	1.6	1.8
25	26	−18	28	−12	3.2	3.4
50	39	−23	40	−18	4.7	5.0
75	62	−40	63	−34	7.3	7.6
100	93	−75	95	−71	12	12
125	151	−306	132	−118	18.7	17.3
150	181	−317	166	−169	22.5	21.2
175	221	−406	210	−229	26.9	25.9
200	287	−458	257	−301	36.4	30.6
225	365	−521	314	−375	44.9	36.8
250	410	−540	379	−447	49.0	44.9

[a] Average voltages of 6th cycle were used as a reference voltage.

ADVANCED
SCIENCE NEWS
www.advancedsciencenews.com

ADVANCED
ENERGY
MATERIALS
www.advenergymat.de

Figure 10. Overview of the cycling data of full cells (25 °C) containing a thin Li-metal anode and different CAMs at 25 °C; a) NMC111; b) NMC622; c) NMC811 and NMC811 + 0.7 × 10⁻³ M HBFEP; d) NMC111 with a reduced amount of electrolyte; in this case, the cells with pristine Li foil could not be cycled. The orange lines correspond to the State-of-Health of 80% of the different cells with the associated numbers of cycles until this status is reached. **Figure 11** also shows the Electrolyte weight-to-capacity ratio and the current density of the cells (green). Quadruplicates were tested for each series of cells.

highly reactive surface-Ni^{4+} ions,[73] that induce consumption of the electrolyte, gas evolution, formation of an insulating interphase with consumption of active material.[54,74,75] Each of these processes in turn results in a loss of capacity, especially at high voltages.[76]

3.3. Testing of the Coated Electrodes in Realistic Full Cells

The emphasis of the following measurements focused on implementing adapted cycling conditions for realistic LMB full cells (see Section S7, Supporting Information). Note that the simple alteration of the electrolyte amount and thickness of the Li-metal anodes in Figure S10 (Supporting Information) results in an extension of the cell's lifetime from 30 cycles to almost 300 cycles without any further treatment of the Li anode and identical cycling protocol. This critical interplay of cell parameters is often underestimated for LMBs. Furthermore, evaluating cycling data is barely possible, if not full cycling parameters are given. Favorably, a series of recent publications provide good guidelines regarding electrochemical measurements for battery applications, which were adhered to in this work.[40,50,77]

Figure 10 shows the cycling data of our realistic full cells, including a 48 µm thin Li-metal foil and a reduced electrolyte weight to cell capacity ratio (26.4–45.5 g Ah). The effect of the HBFEP treatment (**LF005H4**, see Table 1) and the corresponding application of a LiBFEP layer on the lithium foil was first tested with stable low nickel NMC111, followed by NMC622 and NMC811 CAMs of higher Ni-content. The cycling tests (Figure 10a–d) indicate superior performance, and the application of LiBFEP enables stable cycling (0.05-HBFEP) with a threefold delayed onset for the capacity drop (Figure 10a) for cells with NMC111 cathodes. Also, NMC622 and NMC811 full cell cycling data (Figure 10b,c) show a delayed onset for the capacity drop during the course of the cycling. Cells with NMC622 and modified LMAs reach an improvement of 80% versus the untreated reference and almost a doubling of the lifetime is possible with NMC811 cathodes. The extension of the cell's lifetime appears to be strongly related to the CAM, probably attributed to side reactions with the electrolyte and structural changes of the CAM during cycling. As an extension, full cells with NMC111 and further reduced electrolyte amount were built (Figure 10d). The data with a capacity drop after 60 cycles indicate a reduced effect of the LiBFEP-coating used under these electrolyte scarce conditions in comparison to the cycling of NMC111 cells in Figure 10a. By contrast, it was impossible to cycle cells with untreated Li anodes under the same electrolyte scarce conditions[78] as in Figure 10d. This shows the benefit of the HBFEP treatment, which holds for all cycling configurations. Hence, the full-cell lifetime extension reaches up to 285% for NMC111 cathodes, thus confirming the positive properties of the LiBFEP-coating in full cells and under realistic conditions. Note that all cycling data was obtained by measuring quadruplicate cells and those with HBFEP-treated LMAs perform better than the pristine ones (Figure 10a–d). Even
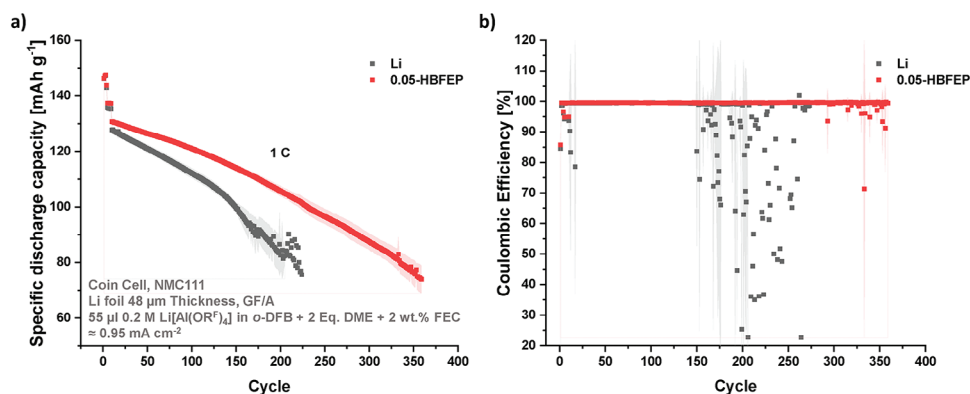
Figure 11. a) Cycling data of full cells (25 °C) containing a thin Li-metal anode and a 0.2 M Li[Al(OR^F)$_4$] in o-DFB + 2 Eq. DME and 2 wt% FEC; b) coulombic efficiencies of the full cells. Quadruplicates were tested for each series of cells.

considering the error ranges, the cycling data show the superior performances of the HBFEP-treated LMBs also considering the error ranges confirming a real improvement in the cell's lifetime. Figure 10c also shows the full-cell cycling data of LMBs with both, HBFEP-treated NMC811 cathodes and LMAs. In this case, the lifetime of the full cells is slightly extended up to 76% and after 37 cycles a significant capacity drop occurs rather than after 21 cycles, as with the untreated electrodes. Figure S12 (Supporting Information) indicates that the main contribution of the improvement in the cell's lifetime results from the HBFEP treated LMAs, since full cells with HBFEP-treated NMC811 cathodes only show a similar lifetime to full cells with untreated electrodes. Apparently, and due to the shorter lifetime of the full cells, the life-prolonging effect of HBFEP-treated NMC811 cathodes differentiating in half cells after 80 cycles (Figure 9a) does not does not yet dominate.

3.4. Full Cells in Low-Polarity, Low-Concentration Electrolyte

One possible reason for the limited lifetime of the HBFEP-coated Li foil in LMBs with carbonate-based electrolyte, is the dissolution of the (very sparingly soluble) LiBFEP. Hence, to further decrease LiBFEP-dissolution in the system, the novel low-concentration and low-polarity electrolyte DFB02 was tested in LMBs. It consists of a 0.2 M solution of lithium perfluorotertbutoxyaluminate (Li[Al(OR^F)$_4$]; R^F = -C(CF$_3$)$_3$) in 1,2-difluorobenzene (oDFB), a polar (ε_r = 14.2 at 25 °C),[79] but almost non-interacting low viscosity solvent (η = 0.69 mPa s at 23 °C, compared to L57 (EC/EMC 3:7 wt%) η = 1.11 mPa s at 20 °C).[80] The [Al(OR^F)$_4$]$^-$ anion is a prime example of a weakly coordinating anion (WCA), where the negative charge is distributed evenly over the entire molecular ion to inhibit ion-pair formation.[81,82] In addition, 2 wt% fluoroethylene carbonate (FEC) was added to DFB02 to improve the compatibility of the electrolyte system with the electrode interfaces/interphases. Lastly, 2 equivalents of DME per Li$^+$ ion act as bidentate ligands in compact [Li(DME)$_2$]$^+$ units and enable fast bulk ion mobility in the low-viscosity electrolyte solution (cf. to the else formed large Li(carbonate)$_4$]$^+$ ion).[83,84] The complexation of the Li$^+$ ions with DME in DFB02 reduces the formation of contact ion pairs (CIP) or aggregate ions and increases the ionicity of the electrolyte to almost 100%. By con-

trast, the LP57 electrolyte has a reduced ionicity of 35–40% with a large fraction of CIPs.[85–87] Additionally, the large size of the [Al(OR^F)$_4$]$^-$ anion increases the solubility through the low lattice energies of its salts. An overview of conductivity and cyclic voltammetry of the DFB02 electrolyte is given in Figure S13 (Supporting Information) and Figure 11 shows the full cell cycling data with the DFB02 electrolyte with and without LiBFEP-coating.

Figure 11a indicates a stable performance of the full cells with the low-concentration electrolyte. Compared to the cells with LP57, a sudden capacity drop is absent, but the capacities drop slowly over several hundred cycles. The LiBFEP-coating (**LF005H4**, see Table 1) improves the full-cell performance, with 80% capacity retention after 177 cycles. Without HBFEP treatment, capacity retention reaches 80% at cycle 119, offering a 49% improvement by LiBFEP-coating. The coulombic efficiencies (CE) (Figure 11b) of all cells remain with stable cycling up to 150 cycles at 99.5%. Thereafter, strong CE-fluctuations accompanied by a dropping/scattering capacity were observed for the pristine cells, probably related to the (erratic) formation of short circuits in the different cells. By contrast, the cells with the LiBFEP-modified LMAs show such a—less pronounced—behavior only after 300 cycles. Even after 350 cycles 54% of the initial capacity was retained. Overall, the compatibility of the only 0.2 M DFB02 electrolyte with LMAs is enhanced compared to the 1 M carbonate-based LP57 electrolyte. Even the absolute capacities at 1 C rate are close to those obtained with five time more concentrated LP57.

What causes the improved stability and performance of the low-concentration DFB02? An anion-derived SEI appears unlikely, since the (electro-)chemically very robust [Al(OR^F)$_4$]$^-$ WCA was used (stable up > 5.5 V versus Li/Li$^+$).[81] The coordination of two molecules of DME to the Li$^+$ ion should result in the formation of a DME-only solvation environment around the Li$^+$ ion. DME itself is not known to support the generation of a stable SEI, whether as a mediator nor its reduction products.[29,88] With its inferior ligand properties, o-DFB should not compete for presence in the solvation shell compared to DME. The X-ray structure confirmed coordination of DME in the LiBFEP coordination polymer, which was weak and fully removable under vacuum.[42] Consequently, the overall properties of the 0.2 M Li[Al(OR^F)$_4$] solution in o-DFB seem to prevent the decomposition of the

electrolyte and the LMA during cycling. The absence of oxidative and reductive currents within the applied potential window of 0 to 4.6 V versus Li/Li⁺ (Figure S13, Supporting Information) indicates good stability of the electrolyte. Also, the absence of large quantities of carbonate solvents in the DFB02 electrolyte compared to LP57 appears to have a positive influence on the performance, as those induce formation of an unstable carbonate-derived SEI on Li-metal.[26,89–93] By contrast, the cycling data with the DFB02 electrolyte indicate a sufficient stabilization of the LMAs interface/interphase by the artificial LiBFEP-coating, possibly supported by FEC addition. With NMR-measurements the solubility of the artificial LiBFEP-SEI was investigated by immersing a HBFEP-treated Li-metal anode in the DFB02 electrolyte. After 24 h, the ^{31}P-NMR-spectra of this liquid did not include any soluble phosphorous products. To test the influence of FEC addition to the LP57 electrolyte, control cells with and without FEC were built (Figure S14, Supporting Information). Their performance is improved by the addition of FEC only, but the extension of the lifetime is much smaller than with the DFB02 electrolyte. Hence, the addition of FEC is not the primary reason for the superior performance and stability of the DFB02 electrolyte in LMBs.

Also compared to literature, the performance of the low-concentration DFB02 electrolyte in combination with the LiBFEP-coating is remarkable. Hitherto, CEs ≥99.5% were only reached in HCE with concentrations of the conducting salt up to 7 м or in electrolyte systems based on liquefied sulfur dioxide.[94] The novel low-concentration electrolyte economically profits from the low concentration of the conducting salt and the cheap components compared to HCE or alternative electrolytes.

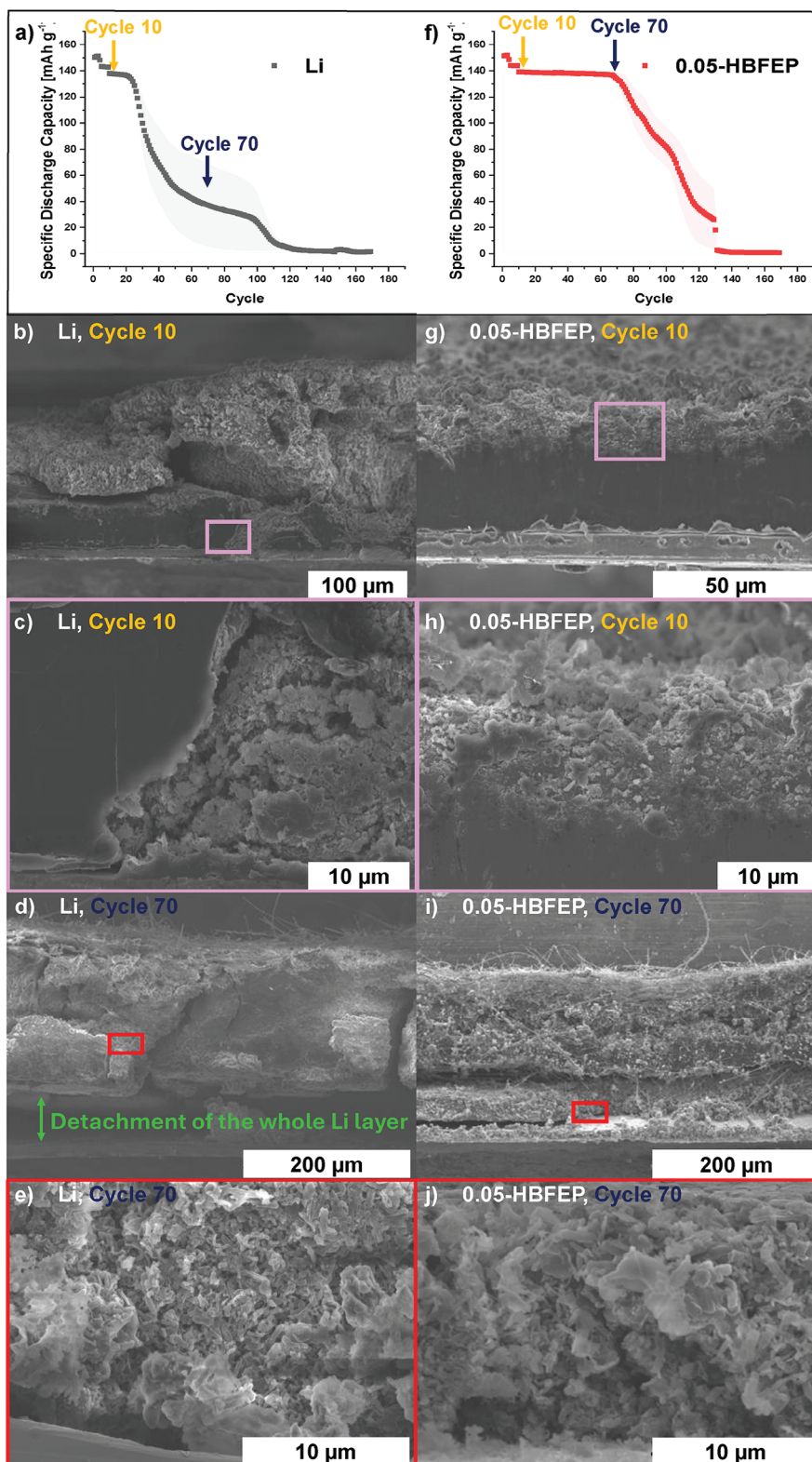## 4. Post-Mortem Investigations of the Li-Metal Anodes

To further investigate the performance of HBFEP-treated Li-metal anodes, NMC111 full cells were built with and without coating, cycled, and opened after 10 and 70 cycles in an argon atmosphere and transferred under inert conditions to the electron microscope. **Figure 12a,f** shows the cycling data of NMC111 full cells built identical to those opened. As expected from Figure 10a, cells containing untreated LMAs exhibit a strong capacity drop after 20 cycles with almost no capacity left after 40 cycles, while HBFEP-treated anodes enable stable cycling for at least 80 cycles. The cross-section SEM images of the LMAs are shown in Figure 12b,g and reveal huge differences, even after only 10 cycles: the untreated LMAs in Figure 12b,c are severely deteriorated with partial pulverization including the formation of dead lithium embedded in a porous layer. Figure 12b shows a second layer underneath the porous layer. Based on the contrast between the porous layer and the morphology, this second layer is metallic lithium. Figure 12c shows the magnification of the lower parts of the untreated LMA (pink box, Figure 12b) after 10 cycles. Figure 12c displays thin, needle-like structures near the Cu current collector foil, indicating at least partial pulverization of the whole LMA even after 10 cycles. By contrast, the cross-section image of the HBFEP-treated cell in Figure 12g indicates an almost intact electrode-structure after 10 cycles. A thin, porous layer is visible in Figure 12h (pink box, Figure 12g)

on top of a homogenous and dense layer of metallic lithium, similar to the non-cycled HBFEP-treated LMAs. The thickness of the HBFEP-treated anode remains at about 50 μm after 10 cycles, whereas the thickness of the untreated anode partially reaches up to 200 μm due to fragmentation. After 70 cycles, the untreated LMA shows a complete breakdown of their structure (Figure 12d), i.e., only a thick, porous layer is present without any visible metallic lithium/a lithium reservoir. Furthermore, the cross-section exhibits bright spots on the surface attributed to isolated dead lithium particles and the complete pulverization of the anode structure due to the reduced electronic conductivity within the deteriorated lithium structure. Under these circumstances, the electron beam from the electron microscope can cause the charging effects. By contrast, after 70 cycles the HBFEP-treated anode in Figure 12i shows only a smaller degree of deterioration. Overall, the anode structure appears to be intact. Three layers are visible; the top layer consists of a porous structure containing some glass fibers of the separator, giving strong hints of the deterioration of the upper parts of the anode. A second layer of the cross-section exhibits a different morphology compared to the top layer (cf. contrast) and indicates the presence of metallic lithium with a corresponding lithium reservoir. Figure 12e shows the magnification of the lower parts of the untreated Li anode (red box, Figure 12d) after 70 cycles. The visible structures confirm the impression of the previous figures, with thin, fibrous, and needle-like substructures and deposits. Figure 12e further supports the disappearance of the Li reservoir, while the structure has completely corroded and deteriorated. Literature stresses that with thinner structures, more severe degradation occurred at the Li anodes.[63,95] Figure 12j shows the analogous magnification of the lower parts of the HBFEP-treated Li anode (red box, Figure 12i) after 70 cycles. Overall, smoother and thicker substructures and deposits are evident, indicating the presence of at least a partial Li reservoir and less deterioration of the Li anode. The cross-sections of cycled full cells are in good agreement with those of the Li-Li symmetrical cell (Figure S6, Supporting Information). The direction of the deterioration and pulverization of full cell LMAs emanate visibly from the electrode/electrolyte interface toward the lithium bulk and the copper current collector.[19,96] A dense structure is visible after 21 cycles in Li-Li symmetrical cells with an additional porous, mossy layer on top of the electrode. The contrast of the dense structure indicates the presence of metallic lithium.[97]

With the LiBFEP-coating stabilizing the LMA structure and inducing superior plating and stripping of lithium, the reduced electrolyte is consumed and, hence, the generation of dead lithium is inhibited.[19,51,96,98] Initiating a life-prolonging effect and retarding the capacity drop of the full cells. The porous layer generated from HBFEP treatment (Figures 3g and 4a) also acts favorable by an increased electrode surface area and, hence, decreased current density, resulting in less lithium deposition per active electrode surface.[21,26]

5. Time-of-Flight Secondary Ion Mass Spectrometry (ToF SIMS)

Further investigations of the LMAs were conducted via ToF-SIMS measurements.

2403195 (13 of 21)

ADVANCED
SCIENCE NEWS

www.advancedsciencenews.com

ADVANCED
ENERGY
MATERIALS

www.advenergymat.de

Figure 12. Exemplary cycling data of full cells; a) cells without HBFEP-treated anodes; f) cells with HBFEP-treated anodes. b–e) SEM cross-section images of cycled Li-metal anodes without HBFEP after 10 and 70 cycles. g–j) SEM cross-section image of cycled HBFEP-treated Li-metal anodes after 10 and 70 cycles; c,h) show the area of magnification in the pink boxes of cycled LMAs after 10 cycles visible in b,g); e,j) show the area of magnification in the red boxes of cycled LMAs after 70 cycles visible in d,i).
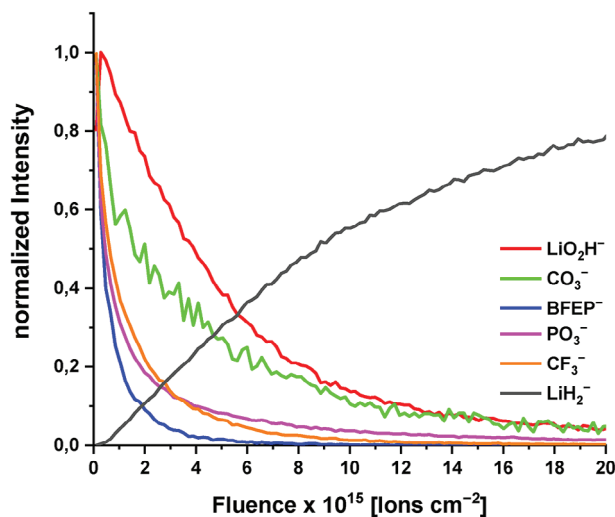
2403195 (14 of 21)

**ADVANCED
SCIENCE NEWS**

www.advancedsciencenews.com

**ADVANCED
ENERGY
MATERIALS**

www.advenergymat.de

Figure 13. Depth profiling of a HBFEP-treated LMA with Ar_{1500}^+-clusters.

5.1. Static Mode

The uppermost layer of an untreated LMA confirmed the presence of white[99] and silicon oils in the static mode (Figure S15, Supporting Information), already evident from the ATR-IR measurements (Figure 3). The untreated LMA (Figure S15, Supporting Information) includes an oxygen-containing layer made from LiOH, Li_2O, and Li_2CO_3. Before analyzing the HBFEP-treated (**LF005H4**, see Table 1) Li-metal foil, a reference sample of LiBFEP was measured, giving a signal at a mass-to-charge ratio (m/z) of 260.97 (= $PO_4C_4H_4F_6^-$, short: $BFEP^-$). This $BFEP^-$ signal is also visible in the static SIMS of the HBFEP-treated LMA (Figure S15, Supporting Information), confirming the presence of LiBFEP.

5.2. Dynamic Mode

The depth profile of the artificial LiBFEP-based SEI was assessed by dynamic measurements shown in **Figure 13** that plots the ion intensities over the course of the depth profiling, determined with the same secondary ions as previously used for the untreated LMA. At the beginning of the sputtering process, the intensity of the $BFEP^-$ signal, concomitantly with that of the PO_3^- and CF_3^- secondary ions, is decreasing rapidly, indicating a thin layer of LiBFEP on the surface (Figure 13).

By contrast, the proportion of detected LiH_2^- ions increases continuously during the sputtering process and is indicative of the presence of metallic lithium. The secondary ions CO_3^- and LiO_2H^- are detected right from the beginning of the sputtering process, agreeing with the presence of Li_2CO_3 and $LiOH/Li_2O$ in the upper layer of the SEI. The signals of CO_3^- and LiO_2H^- exhibit a noisier behavior. Since Figure 13 plots the normalized intensities of the secondary ions, this agrees with lower absolute intensities, if compared to the BFEP-associated secondary ions PO_3^- and CF_3^-. BFEP-associated ions show a sharp intensity drop, but carbonate- and oxide/hydroxide-associated ions exhibit a less pronounced drop. The signals of the oxide/hydroxide ions seem to have the highest intensity in deeper

areas of the SEI structure where the LiH_2^- intensity already increases. This suggests the thickness of the carbonate layer to be lower than the $Li_2O/LiOH$ layer. The following structure of the artificial SEI layer from the inside to the outside is plausible: The metallic lithium is followed by an inorganic Li_2O/LiF layer and a hybrid layer consisting of mainly LiBFEP and little $LiOH/Li_2O/Li_2CO_3$ presents the outside. These results agree with the ATR-IR measurements and our earlier X-ray photoelectron spectroscopy (XPS)-measurements[42] that suggested a strong reduction of the $LiOH/Li_2CO_3$ layer at the top of the coating. ToF-SIMS measurements would estimate the thickness of the layers to be a few nm with a total thickness of the SEI approaching about 100 nm. By contrast, SEM- and EDX-measurements of the 0.05-HBFEP treated Li-foil show a porous layer with a thickness of almost 10 μm (Section 2.3), which is also supported by calculations based on the NMR-titration and the crystal density of LiBFEP (6 μm). This contradiction to the ToF-SIMS measurements may arise from different penetration depths of the ion beam due to the porous surface. When plotting against the fluence, a flat surface of the lithium-coating is assumed. Hence, these simplifications could result in a distortion of the depth correlation. Nevertheless, the depth profiles show the presence of metallic lithium at lower fluences for HBFEP-treated Li-metal anodes, which indicate a thinner native oxide layer with an additional layer of LiBFEP.
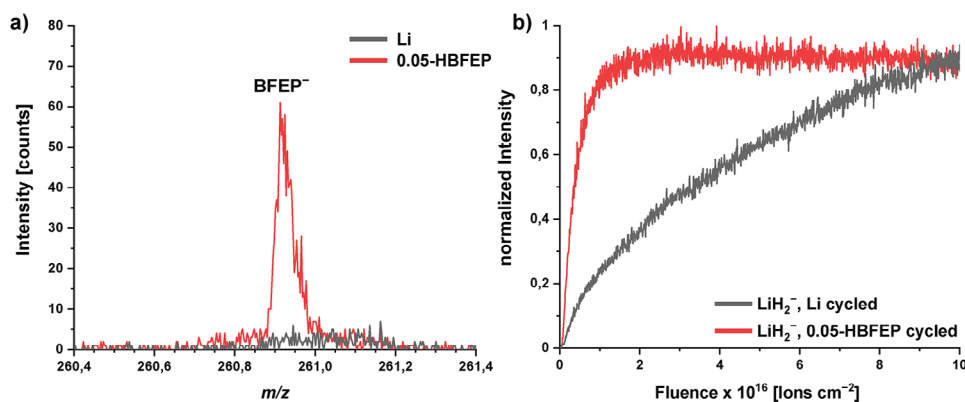
5.3. Dynamic Measurements After Cycling

To study the composition of the SEI of the Li-metal anodes after cycling, Li-Li symmetrical were opened in inert conditions with the same precautions as for the SEM measurements. **Figure 14** shows the sputtering results of these Li-metal anodes after 21 cycles. Figure 14a confirms the existence of LiBFEP after cycling and demonstrates resistance of LiBFEP to the cycling conditions. The course of the intensity of the LiH_2^- signal from the HBFEP-treated anode, attributed to the presence of metallic lithium, exhibits an immediate increase at a low fluence and stays constant during the ongoing sputtering process (Figure 14b).

By contrast, the untreated anode shows only a slowly increasing intensity of the secondary ion LiH_2^-, reaching similar values to the coated anode only at a high fluence of 10×10^{16} ions cm^{-2}. This indicates that during the sputtering process, metallic Lithium was present near the cycled HBFEP-treated electrode surface, while a thick layer of decomposition products seems to be present on the untreated electrode. Thus, the ToF-SIMS measurements confirm the deductions from the SEM measurements (Figure 12, Figure S6, Supporting Information) and suggest a reduced decomposition of the electrolyte on the coated electrode.

6. Electrochemical Impedance Spectroscopy (EIS)

The thin Li-metal foil electrodes used in our electrochemical measurements, were further evaluated with electrochemical impedance spectroscopic (EIS-) measurements in the following section.

ADVANCED
SCIENCE NEWS

www.advancedsciencenews.com

ADVANCED
ENERGY
MATERIALS

www.advenergymat.de

Figure 14. a) Spectra of the BFEP$^-$-signal of a cycled untreated Li-metal foil (Li, black) and a cycled HBFEP-treated Li-metal foil (0.05-HBFEP, red) after 21 cycles (Static SIMS). b) Depth profiles of the LiH$_2^-$-signal of a cycled untreated Li-metal foil (Li, black) and HBFEP-treated Li-metal foil (0.05-HBFEP, red) after 21 cycles, dynamic measurements with 10 keV Ar$_{1500}^+$-clusters.
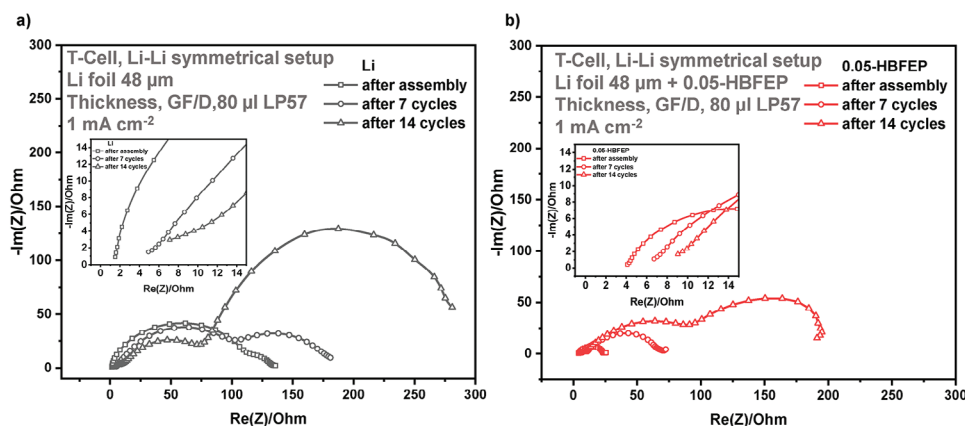
6.1. Nyquist Plots

Figure 15 shows the EIS spectra of Li-Li symmetrical cells containing a 48 μm thin Li-metal foil recorded during the cycling of the cells. High impedance is visible for the untreated LMA after the assembly of the 3-electrode T-cells (Figure 15a). Cycling leads to a strong drop of the impedance after seven cycles, indicating first the presence of a poorly disordered Li-ion conducting surface layer after the assembly and its subsequent transformation into a more conductive layer with lower impedance. Upon further cycling, the spectra shift to higher impedances. The native oxide layer on LMAs (Figures 3 and 14), may be responsible for this.[99,100] By contrast, the spectra of the HBFEP-treated LMAs (**LF005H4**, Table 1) in Figure 15b exhibit directly after the assembly a low impedance. This agrees with the formation of a Li-ion conducting surface layer and at least the partial removal of the native oxide layer. In the subsequent cycles, the EIS spectra slightly shift toward higher impedance values. Yet, the extent of the increase is much smaller than for the cell with the untreated LMA.

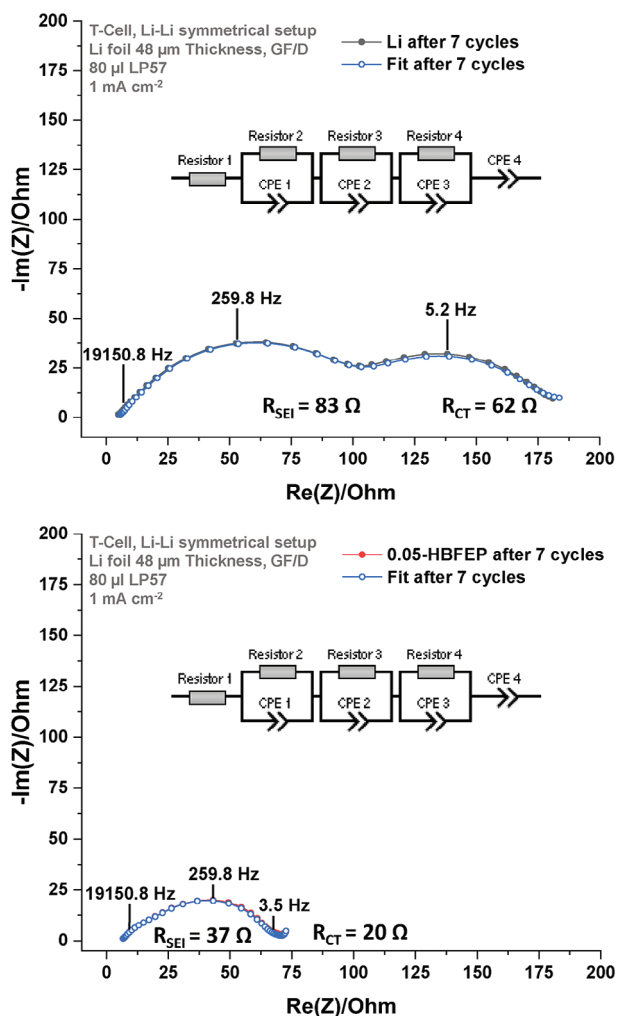Interestingly, during cycling with untreated electrodes, the high-frequency part (>5 kHz) with the intercept of the x-axis is also shifting to higher impedances. This high-frequency part represents fast processes with short time constants, e.g. contact and electrolyte resistances.[101] The HBFEP-treated cells show a significantly lower shift of the high-frequency part during the cycling, even after 14 cycles. This supports all previous conclusions on the nature and action mode of the LiBFEP-based artificial SEI.

To further evaluate the processes during the electrochemical reaction, the frequency ($\omega_{-\text{Im}(Z)_{max}}$) at the maximum of the imaginary part ($-\text{Im}(Z)$) of the independent semicircles was determined. **Figure 16** shows the spectra of the different LMAs (Counter Electrode) including the peak frequencies of every semicircle. The frequencies of the first semicircle in the range >10^5 Hz indicate an electronic process. The existence of contact resistance between the current collector foil and the CAM was designated as the cause of this electronic process.[102,103] Similar observations can be made for graphite-based anodes.[104] With our focus on thin LMAs, conventional electrodes were not used, and a direct comparison of the EIS-measurements with different electrodes is to some extent critical. Nevertheless, since the lithium was applied on the current collector foil by a rolling process, a reduced electrical conductivity between the metal foil and the lithium layer may be possible. In the midfrequency

Figure 15. Nyquist plots of Swagelok type Li-Li symmetrical cells during the cycling at 1.0 mA cm^{-2}; a) using untreated Li-metal foil, including a magnified area at low impedances; b) using HBFEP-treated (0.05HBFEP) Li-metal anodes. The EIS spectra were measured from 100 kHz to 100 mHz with a perturbation of 10 mV at 25 °C in 3-electrode T-cells.

ADVANCED
SCIENCE NEWS

www.advancedsciencenews.com

**ADVANCED
ENERGY
MATERIALS**

www.advenergymat.de

Figure 16. Nyquist plots of Swagelok type Li-Li symmetrical cells after 7 cycles, including the peak frequencies of the different processes; comparing untreated Li-metal anodes and HBFEP-treated (0.05HBFEP) Li-metal anodes. Figure 16 also shows the fitted spectra of the LiLi symmetric cells, including the equivalent circuit for the fits. The EIS spectra were measured from 100 kHz to 100 mHz with a perturbation of 10 mV at 25 °C in 3-electrode T-cells.

region (<10 kHz) a depressed semicircle is visible in both spectra (Figure 16).

The peak frequencies of 259.8 Hz, both for Li and 0.05-HBFEP, indicate an ion-related process, which may be caused by the migration of the Li⁺ ions through the SEI layer.[105] A comparison of both spectra shows the superior performance of the HBFEP-treated to the untreated anode with lower resistances, attributed to the action of the artificial LiBFEP-based SEI. A third semicircle was identified in the low-frequency region of the spectra. With peak frequencies of 5.2 Hz (Li) and 3.5 Hz (0.05-HBFEP), another ion-related process with significantly lower time constant seems to cause the semicircle. Semicircles in similar frequency regions were attributed to charge-transfer processes at the lithium interface.[105] The EIS measurements also imply a substantial influence of the composition of the lithium surface on the charge-transfer resistance during the cycling since the low-

frequency regions of the different LMAs exhibit different behaviors, as already evident in the EIS spectra directly after cell assembly.

Figure 16 also contains the fits of the EIS-spectra of the cells after seven cycles, which agree well with the spectra, especially at high to mid frequencies, and confirm the significantly lower resistance for the 0.05-HBFEP cells (Table S1, Supporting Information). There are slight deviations at low to very low frequencies (<1 Hz), which may relate to diffusion processes that exceed the scope of this work. In addition, variable temperature EIS-measurements (Figure S16, Supporting Information) between −10 °C and +50 °C confirmed the assignments of the semicircles to the different electronic and ionic processes and according to Figure 16.[106,107]

The EIS measurements resolved individual processes at the electrode/electrolyte interface and showed the presence of one electronic process in combination with two more ionic processes. These measurements determined the real impact of the HBFEP treatment, especially on the ionic processes of LMAs during the cycling, and confirmed all previous assumptions: The resistances R_{SEI} (R3) and R_{CT} (R4) are significantly lower (Figure 16; 82 Ω → 37 Ω; 62 Ω → 20 Ω) for the HBFEP-treated LMAs with values of 30–40% of the untreated LMA after seven cycles.

7. Conclusion

This work provides a detailed overview of the performance of thin LMAs in realistic lithium-based full cells. The ionic coordination polymer LiBFEP is formed in an immersion process and acts as an artificial SEI. Three more phosphoric acid derivates with different fluoroalkyl chains were synthesized and applied on the LMAs by immersion, yet performed inferior in symmetric Li-Li cells. This immersion process was also applied to the nickel-rich CAMs NMC 811 and NMC850510. Basic surface species—inherent to nickel rich CAMs—can be removed and converted in an acid–base reaction with HBFEP to a LiBFEP-coating on the surface of the NMC particles. Half-cell tests showed the HBFEP-treated NMC cathodes to work favorable, with suppressed polarization throughout the cycling and reduced constant voltage charging times.

Extended electrochemical cycling tests in Li-Li symmetrical cells showed the successful performance of HBFEP-treated thin LMAs. Reduced overpotentials of the artificial SEI induce a life-prolonging effect, almost doubling the lifetime. In full cells, adapted to yield realistic measurements, the artificial SEI works favorably with three NMC-CAMs and the cell's lifetime was up to tripled by using HBFEP-treated anodes. SEM images revealed the structural stabilization of the HBFEP-treated anodes during and after the cycling tests, with the artificial SEI suppressing parasitic reactions and the formation of dead lithium. This was further supported by ToF-SIMS and EIS measurements. EIS enables a quasi-in-operando investigation of the Li-metal anodes during the cycling of the cells and a deconvolution of the different processes confirmed beneficial effects, especially for ion-related processes and supporting the presence of a stabilizing, protective artificial SEI of a Li-ion coordination polymer.

Hence, an artificial LiBFEP-based SEI improves the performance of LMBs by a simple immersion process and also functions on the CAM side. The results may enable a pathway toward

**ADVANCED
SCIENCE NEWS**

www.advancedsciencenews.com

**ADVANCED
ENERGY
MATERIALS**

www.advenergymat.de

large-format LMBs and the associated implementation into an industrial production process.

8. Syntheses and Methodologies

All manipulations were carried out in an argon-filled (99.999%) glovebox (GS MEGA Line 3), where the oxygen content was <3 ppm and the water content was <1 ppm.

Syntheses: Compound **1**: Tris(2,2,2-trifluoroethyl) phosphate (3.4 g, 2.2 mL, 10 mmol, 1.0 eq.) [>96%, TCI] and water (198 µL, 11 mmol, 1.1 eq.) were mixed and stirred at 321 K for 72 h. All volatile components were removed under reduced pressure and the residue was dried in a vacuum (3×10^{-3} mbar) at 323 K. Bis(2,2,2-trifluoroethyl)-hydrogen phosphate (1.2 g, 4.6 mmol, 47%) was obtained as colorless solid with a purity of 97%. The side product was $[(HO)_2P(O)(OCH_2CF_3)]$ (3%). Furthermore, Compound **1** was synthesized with the anhydrous route. 2,2,2-Trifluoroethanol (79.5 g, 60.0 mL, 840 mmol, 8.07 eq.) was cooled to 243 K. P_4O_{10} (29,6 g, 104 mmol, 1.00 eq.) was then slowly added to the alcohol. The suspension was stirred overnight at 293 K. Afterwards, the solution was refluxed at 383 K for 3 h. A colorless liquid was obtained, and the excess alcohol was then removed under vacuum conditions (3×10^{-3} mbar) at 293 K. To further increase the purity, the raw product was distilled twice in vacuo from one Schlenk flask (403 K) to another connected by a knee, while the second one was cooled to 243 K.[43] Bis(2,2,2-trifluoroethyl)-hydrogen phosphate (20.8 g, 79.4 mmol, 19%) was obtained as colorless solid with a purity of 94.5%. The side products were $[(HO)_2P(O)(OCH_2CF_3)]$ (5%) and $[(O)P(OCH_2CF_3)_3]$ (0.5%). HBFEP used in this work originates from the anhydrous syntheses.

Compound **2**: 1H,1H,2H,2H-perfluoro-1-octanol (10.7 g, 6.50 mL, 29.4 mmol, 1.00 eq.) was cooled to 273 K. P_4O_{10} (1.05 g, 36.9 mL, 1.26 eq.) was then slowly added to the alcohol. Afterward, the suspension was refluxed at 463 K for 1 h. A colorless liquid was obtained, and the excess alcohol was then removed under vacuum conditions (3×10^{-3} mbar) at 333 K. For purification, the viscous liquid was dissolved in (18 mL) diethyl ether (Et_2O) and washed with water. A colorless solid was obtained by removing diethyl ether. To further increase the purity, the product was crystallized from a cooled solution in diethyl ether. This procedure was repeated six times. Bis(3,3,4,4,5,5,6,6,7,7,8,8,8-tridecafluorooctyl)-hydrogen phosphate (0.941 g, 1.18 mmol, 8.27%) was obtained as colorless solid with a purity of 80%. The side product was $[(HO)_2P(O)(O(CH_2)_2-(CF_2)_5CF_3)]$ (20%).

Compound **3**: Tris(2,2,3,3,4,4,5,5-octafluoropentyl) phosphate (10.6 g, 6.00 mL, 14.3 mmol, 1.00 eq.) was mixed with water (0.283 g, 0.283 mL, 15.7 mmol, 1.10 eq.) and stirred at 323 K for 14 days. Afterward, the mixture was dried in a vacuum (3×10^{-3} mbar) at 323 K for 4 h. Bis(2,2,3,3,4,4,5,5-octafluoropentyl)-hydrogen phosphate (4.61 g, 8.76 mmol, 61.3%) was obtained as a highly viscous colorless oil with a purity of 72%. The side products were $[(HO)_2P(O)(O(CH_2)-(CF_2)_3CF_2H)]$ (5%) in combination with not converted triester (23%).

Compound **4**: To freshly dried 1,1,1,3,3,3-hexafluoro-2-propanol (92.8 g, 58.1 mL, 552 mmol, 8 Eq) P_4O_{10} (19.6 g, 69.0 mmol, 1 Eq) was added in smaller portions at 271 K. The mixture was allowed to warm up to room temperature and stirred for 16 h. Afterwards, the solution was refluxed at 333 K for 3 h.

Excessive alcohol was removed under reduced pressure. The residue was distilled in vacuum at 393 K oil bath temperature whereas the receiver flask was cooled to 253 K. After sublimation of the distillate in vacuum at 343 K oil bath temperature, bis(1,1,1,3,3,3-hexafluoro-2-propyl)-hydrogen phosphate (4.58 g, 11.5 mmol, 4.17%) was obtained as colorless solid with a purity of 95%. The side products were higher phosphates or cyclic phosphates (5%).

Characterization Methods: ATR-IR spectra were recorded inside the glovebox with an Alpha FT-IR spectrometer (Bruker) using an ATR diamond unit. To ensure sufficient contact between the samples and the diamond unit, the samples were slightly pressed with a stamp onto the ATR diamond unit. SEM-EDX images were obtained with a FEG-HRSEM SU8220 (Hitachi) at 25 °C using an accelerating voltage of 5 kV. An Everhart–Thornley detector was used in the secondary electron (SE) mode. The EDX-measurements were done with a XFlash 6-30-detector (Bruker) and the QUANTAX FlatQUAD-detector (Bruker). The accelerating voltage was also set to 5 kV or 18 kV. The samples were prepared and mounted inside the glovebox. The inert transfer of the samples to the SEM was ensured by a specialized sample holder (Hitachi). For the post-mortem investigations, the cells were opened, the Li-metal electrodes extracted from the battery stack, washed in 1 mL EMC for 1 min, and then dried. The samples for the cross-section investigation were cut at −40 °C on a precooled metal cube using a scalpel. The inert transfer was also ensured by a specialized sample holder (Hitachi). ToF-SIMS measurements were carried out on a TOF.SIMS5 device (ION-TOF GmbH, Münster) using Bi^+ primary ions and a reflectron time-of-flight analyzer. A high vacuum system, pressure of $<3 \times 10^{-8}$ mbar, was applied. To enhance the mass resolution, the Bi^+ primary ion source was operated in high current bunched mode, which delivers short Bi^+ primary ion pulses with an energy of 25 keV, a lateral resolution of approx. 4 µm and a target current of 1.4 pA at a 10 kHz repetition rate. For depth profiling, a dual-beam analysis was carried out in interlaced mode: An argon cluster beam, Ar_{1500}^+ with 10 keV energy, was scanned over 300×300 µm^2 whereas the primary Bi^+ beam was scanned over 100×100 µm^2 (64×64 data points).

Nuclear Magnetic Resonance (NMR) Spectroscopy: NMR spectroscopic measurements were carried out with Young's valve NMR tubes to ensure inert conditions during the measurements. To calculate the loading of LiBFEP on the electrode surface, the concentration of HBFEP in the coating solution was determined before and after the immersion process. The difference in the HBFEP concentration was normalized to the overall surface of the electrode(s). The determination was based on an internal *ortho*-Difluorobenzene standard. A Bruker Avance III HD 300 MHz, Bruker Avance DPX 200 MHz, and Bruker Avance II+ Widebore 400 MHz were used as spectrometers to obtain the spectra.

Electrochemical Measurements: Electrochemical measurements were conducted at 25 °C under controlled temperature conditions (Binder KB53) in different cell setups. Li-Li symmetrical cells were tested in a coin cell setup with CR2032 cell format (Gelon, SS316). An amount of 55 µL of electrolyte (LP57, BASF) was added to the cells using a glass fiber separator (Whatman GF/A, Ø 16 mm). Lithium electrodes (Ø 15 mm) were punched out of a thin Li-metal foil (48 µm thickness on

12 μm copper, China Energy Lithium Co., Ltd.) for the cycling tests. The cycling parameters were kept as follows: after 1 h initial rest time the cells were charged and discharged for 1 h with a constant current density of 1 mA cm^{-2} (1 mAh cm^{-2} areal capacity) with a rest time of 3 min in between; the symmetric cell cycling was stopped when a predefined cell voltage was reached (±3 V). Half cells (NMC8505101.7 mAh cm^2, BASF former project) were built in combination with thick lithium electrodes (450 μm) and 90 μL of electrolyte. Whatman GF/D, Ø 16 mm was used as a separator. Half cells and full-cell tests were also carried out in a CR2032 coin cell setup. Thin 48 μm lithium electrodes (Ø 15 mm) were used as anodes and combined with NMC-based cathodes (Ø 14 mm) (NMC111-NMC811) with an areal loading of 1.0 mAh cm^{-2} (CustomCells). The amount of electrolyte and the separator were identical to the symmetrical cells (55 μL LP57, Whatman GF/A, Ø 16 mm). All cells were subjected to three formation cycles at C/10 after a rest time of 10 h, followed by one cycle at C/5 and five cycles at C/2. Afterward, the cells were cycled at 1C for 200 cycles in a CC-CV mode with cutoff voltages at 4.3 and 3.0 V. The current limit during the constant voltage step was set to C/20. The coin cells were tested with a Landt CT3001A or CT3002A multichannel battery tester. Swagelok T-cells (3-electrode setup) were used for electrochemical impedance spectroscopy (EIS) measurements in Li-Li symmetrical cells containing a lithium reference electrode (BASF). Thin 48 μm lithium electrodes (Ø 12 mm) were inserted as anodes (counter electrodes) and cathodes (working electrodes). An amount of 80 μL of LP57 electrolyte was added for the measurements on top of a glass fiber separator (Whatman GF/D, Ø 13 mm). The cycling tests were performed at a current density of 1 mA cm^{-2} with a corresponding areal capacity of 1 mAh cm^{-2}. The symmetric cell cycling was also stopped when a predefined cell voltage was reached (±3 V). The impedance measurements were performed at fixed intervals of seven cycles under potential control (PEIS) with a perturbation of 10 mV at OCV in the frequency range between 200 kHz and 0.1 Hz. Before the measurements, the cells were rested at OCV for 1 h after plating at the working electrode.

Supporting Information

Supporting Information is available from the Wiley Online Library or from the author.

Acknowledgements

Conflict of Interest

The authors declare no conflict of interest.

Data Availability Statement

The data that support the findings of this study are available from the corresponding author upon reasonable request.

Keywords

[1] S. Khalili, E. Rantanen, D. Bogdanov, C. Breyer, *Energies* **2019**, *12*, 3870.

[2] W. F. Lamb, T. Wiedmann, J. Pongratz, R. Andrew, M. Crippa, J. G. J. Olivier, D. Wiedenhofer, G. Mattioli, A. A. Khourdajie, J. House, S. Pachauri, M. Figueroa, Y. Saheb, R. Slade, K. Hubacek, L. Sun, S. K. Ribeiro, S. Khennas, S. de la Rue du Can, L. Chapungu, S. J. Davis, I. Bashmakov, H. Dai, S. Dhakal, X. Tan, Y. Geng, B. Gu, J. Minx, *Environ. Res. Lett.* **2021**, *16*, 073005.

[3] Regulation (EU) 2023/851 of the European Parliament and of the Council of 19 April 2023 amending Regulation (EU) 2019/631 as regards strengthening the CO2 emission performance standards for new passenger cars and new light commercial vehicles in line with the Union's increased climate ambition, **2023**.

[4] Executive Order on Catalyzing Clean Energy Industries and Jobs Through Federal Sustainability, The White House, December **2021**.

[5] X.-B. Cheng, Q. Zhang, *J. Mater. Chem. A* **2015**, *3*, 7207.

[6] W. Xu, J. Wang, F. Ding, X. Chen, E. Nasybulin, Y. Zhang, J.-G. Zhang, *Energy Environ. Sci.* **2014**, *7*, 513.

[7] R. Cao, W. Xu, D. Lv, J. Xiao, J.-G. Zhang, *Adv. Energy Mater.* **2015**, *5*, 1402273.

[8] C. Niu, H. Lee, S. Chen, Q. Li, J. Du, W. Xu, J.-G. Zhang, M. S. Whittingham, J. Xiao, J. Liu, *Nat. Energy* **2019**, *4*, 551.

[9] B. Han, D. Xu, S.-S. Chi, D. He, Z. Zhang, L. Du, M. Gu, C. Wang, H. Meng, K. Xu, Z. Zheng, Y. Deng, *Adv. Mater.* **2020**, *32*, 2004793.

[10] Q.-K. Zhang, X.-Q. Zhang, H. Yuan, J.-Q. Huang, *Small Sci.* **2021**, *1*, 2100058.

[11] H. Wu, H. Jia, C. Wang, J.-G. Zhang, W. Xu, *Adv. Energy Mater.* **2021**, *11*, 2003092.

[12] W. Xue, M. Huang, Y. Li, Y. G. Zhu, R. Gao, X. Xiao, W. Zhang, S. Li, G. Xu, Y. Yu, P. Li, J. Lopez, D. Yu, Y. Dong, W. Fan, Z. Shi, R. Xiong, C.-J. Sun, I. Hwang, W.-K. Lee, Y. Shao-Horn, J. A. Johnson, J. Li, *Nat. Energy* **2021**, *6*, 495.

[13] Z. Wang, Z. Sun, Y. Shi, F. Qi, X. Gao, H. Yang, H.-M. Cheng, F. Li, *Adv. Energy Mater.* **2021**, *11*, 2100935.

[14] X. Gao, Y.-N. Zhou, D. Han, J. Zhou, D. Zhou, W. Tang, J. B. Goodenough, *Joule* **2020**, *4*, 1864.

[15] L. He, Q. Sun, L. Lu, S. Adams, *ACS Appl. Mater. Interfaces* **2021**, *13*, 34320.

[16] S. Xu, K.-H. Chen, N. P. Dasgupta, J. B. Siegel, A. G. Stefanopoulou, *J. Electrochem. Soc.* **2019**, *166*, A3456.

[17] C. Fang, X. Wang, Y. S. Meng, *Trends Chem.* **2019**, *1*, 152.

[18] C. Fang, J. Li, M. Zhang, Y. Zhang, F. Yang, J. Z. Lee, M.-H. Lee, J. Alvarado, M. A. Schroeder, Y. Yang, B. Lu, N. Williams, M. Ceja, L. Yang, M. Cai, J. Gu, K. Xu, X. Wang, Y. S. Meng, *Nature* **2019**, *572*, 511.

[19] K.-H. Chen, K. N. Wood, E. Kazyak, W. S. LePage, A. L. Davis, A. J. Sanchez, N. P. Dasgupta, *J. Mater. Chem. A* **2017**, *5*, 11671.

[20] X.-R. Chen, C. Yan, J.-F. Ding, H.-J. Peng, Q. Zhang, *J. Energy Chem.* **2021**, *62*, 289.

[21] X. Zhang, Y. Yang, Z. Zhou, *Chem. Soc. Rev.* **2020**, *49*, 3040.

[22] N.-W. Li, Y.-X. Yin, C.-P. Yang, Y.-G. Guo, *Adv. Mater.* **2016**, *28*, 1853.

[23] Z. Yu, Y. Cui, Z. Bao, *Cell Rep. Phys. Sci.* **2020**, *1*, 100119.

[24] T.-H. Kim, J.-H. Lim, J.-H. Yim, J.-W. Lee, *J. Alloys Compd.* **2023**, *959*, 170424.

[25] Y. Xiao, R. Xu, L. Xu, J.-F. Ding, J.-Q. Huang, *Energy Mater.* **2022**, *1*, 100013.

[26] J.-F. Ding, Y.-T. Zhang, R. Xu, R. Zhang, Y. Xiao, S. Zhang, C.-X. Bi, C. Tang, R. Xiang, H. S. Park, Q. Zhang, J.-Q. Huang, *Green Energy Environ.* **2023**, *8*, 1509.

[27] E. Peled, S. Menkin, *J. Electrochem. Soc.* **2017**, *164*, A1703.

[28] Y. Yamada, M. Yaegashi, T. Abe, A. Yamada, *Chem. Commun.* **2013**, *49*, 11194.

[29] J. Qian, W. A. Henderson, W. Xu, P. Bhattacharya, M. Engelhard, O. Borodin, J.-G. Zhang, *Nat. Commun.* **2015**, *6*, 6362.

[30] S. Chen, J. Zheng, D. Mei, K. S. Han, M. H. Engelhard, W. Zhao, W. Xu, J. Liu, J.-G. Zhang, *Adv. Mater.* **2018**, *30*, 1706102.

[31] Z. Yu, H. Wang, X. Kong, W. Huang, Y. Tsao, D. G. Mackanic, K. Wang, X. Wang, W. Huang, S. Choudhury, et al., *Nat. Energy* **2020**, *5*, 526.

[32] L. Suo, W. Xue, M. Gobet, S. G. Greenbaum, C. Wang, Y. Chen, W. Yang, Y. Li, J. Li, *Proc. Natl. Acad. Sci. U. S. A.* **2018**, *115*, 1156.

[33] R. Zhang, N.-W. Li, X.-B. Cheng, Y.-X. Yin, Q. Zhang, Y.-G. Guo, *Adv. Sci.* **2017**, *4*, 1600445.

[34] Z. Yang, Q. Ruan, Y. Xiong, X. Gu, *Batteries* **2023**, *9*, 30.

[35] Z. Chang, H. Yang, A. Pan, P. He, H. Zhou, *Nat. Commun.* **2022**, *13*, 6788.

[36] H. Wu, L. Chen, Y. Chen, *Sustainable Energy Fuels* **2021**, *5*, 5656.

[37] J. Betz, G. Bieker, P. Meister, T. Placke, M. Winter, R. Schmuch, *Adv. Energy Mater.* **2019**, *9*, 1803170.

[38] X.-Q. Zhang, X.-B. Cheng, X. Chen, C. Yan, Q. Zhang, *Adv. Funct. Mater.* **2017**, *27*, 1605989.

[39] S. Chen, F. Dai, M. Cai, *ACS Energy Lett.* **2020**, *5*, 3140.

[40] H. Kwon, J. Baek, H.-T. Kim, *Energy Storage Mater.* **2023**, *55*, 708.

[41] L. Chen, J. Lai, Z. Li, H. Zou, J. Yang, K. Ding, Y.-P. Cai, Q. Zheng, *Commun. Mater.* **2023**, *4*, 18.

[42] W. Beichel, J. Skrotzki, P. Klose, C. Njel, B. Butschke, S. Burger, L. Liu, R. Thomann, Y. Thomann, D. Biro, S. Thiele, I. Krossing, *Batteries Supercaps* **2022**, *5*, 202100347.

[43] M. Schleep, S. Reininger, P. Eiden, P. Klose, C. Schulz, H. Scherer, S. Laule, S. Bodendorfer, M. Schmidt, A. Garsuch, I. Krossing, *ChemElectroChem* **2016**, *3*, 774.

[44] M. S. Milien, H. Beyer, W. Beichel, P. Klose, H. A. Gasteiger, B. L. Lucht, I. Krossing, *J. Electrochem. Soc.* **2018**, *165*, A2569.

[45] J. Han, L. Kiss, H. Mei, A. M. Remete, M. Ponikvar-Svet, D. M. Sedgwick, R. Roman, S. Fustero, H. Moriwaki, V. A. Soloshonok, *Chem. Rev.* **2021**, *121*, 4678.

[46] T. Mahmood, J. M. Shreeve, *Inorg. Chem.* **1986**, *25*, 3830.

[47] R. E. Banks, *(Hrsg.) Topics in Applied Chemistry*, Springer Science & Business Media; Springer, New York, NY **2013**.

[48] Y. Kim, M. Kim, T. Lee, E. Kim, M. An, J. Park, J. Cho, Y. Son, *Electrochem. Commun.* **2023**, *147*, 107437.

[49] Z. Lin, T. Liu, X. Ai, C. Liang, *Nat. Commun.* **2018**, *9*, 5262.

[50] S. Chen, C. Niu, H. Lee, Q. Li, L. Yu, W. Xu, J.-G. Zhang, E. J. Dufek, M. S. Whittingham, S. Meng, J. Xiao, J. Liu, *Joule* **2019**, *3*, 1094.

[51] J. Liu, Z. Bao, Y. Cui, E. J. Dufek, J. B. Goodenough, P. Khalifah, Q. Li, B. Y. Liaw, P. Liu, A. Manthiram, Y. S. Meng, V. R. Subramanian, M. F. Toney, V. V. Viswanathan, M. S. Whittingham, J. Xiao, W. Xu, J. Yang, X.-Q. Yang, J.-G. Zhang, *Nat. Energy* **2019**, *4*, 180.

[52] H.-J. Noh, S. Youn, C. S. Yoon, Y.-K. Sun, *J. Power Sources* **2013**, *233*, 121.

[53] H.-H. Ryu, K.-J. Park, C. S. Yoon, Y.-K. Sun, *Chem. Mater.* **2018**, *30*, 1155.

[54] F. Schipper, E. M. Erickson, C. Erk, J.-Y. Shin, F. F. Chesneau, D. Aurbach, *J. Electrochem. Soc.* **2017**, *164*, A6220.

[55] J. Kim, H. Lee, H. Cha, M. Yoon, M. Park, J. Cho, *Adv. Energy Mater.* **2018**, *8*, 1870023.

[56] A. Butt, G. Ali, K. Tul Kubra, R. Sharif, A. Salman, M. Bashir, S. Jamil, *Energy Technol.* **2022**, *10*, 2100775.

[57] S. Radloff, R.-G. Scurtu, M. Hölzle, M. Wohlfahrt-Mehrens, *J. Electrochem. Soc.* **2022**, *169*, 040514.

[58] a) L. Ibing, T. Gallasch, A. Friesen, P. Niehoff, A. Hintennach, M. Winter, M. Börner, *J. Power Sources* **2020**, *475*, 228608; b) D. Pritzl, T. Teufl, A. T. S. Freiberg, B. Strehle, J. Sicklinger, H. Sommer, P. Hartmann, H. A. Gasteiger, *J. Electrochem. Soc.* **2019**, *166*, A4056.

[59] a) U. Breddemann, J. Sicklinger, F. Schipper, V. Davis, A. Fischer, K. Huber, E. M. Erickson, M. Daub, A. Hoffmann, C. Erk, B. Markovsky, D. Aurbach, H. A. Gasteiger, I. Krossing, *Batter. Supercaps* **2021**, *4*, 632; b) A. Martens, C. Bolli, A. Hoffmann, C. Erk, T. Ludwig, M. El Kazzi, U. Breddemann, P. Novák, I. Krossing, *J. Electrochem. Soc.* **2020**, *167*, 070510.

[60] W. Yan, S. Yang, Y. Huang, Y. Yang, G. Yuan, *J. Alloys Compd.* **2020**, *819*, 153048.

[61] G. A. Elia, J.-B. Park, Y.-K. Sun, B. Scrosati, J. Hassoun, *ChemElectroChem* **2014**, *1*, 47.

[62] G. Bieker, M. Winter, P. Bieker, *Phys. Chem. Chem. Phys.* **2015**, *17*, 8670.

[63] S. Jiao, J. Zheng, Q. Li, X. Li, M. H. Engelhard, R. Cao, J.-G. Zhang, W. Xu, *Joule* **2018**, *2*, 110.

[64] D. E. Galvez-Aranda, J. M. Seminario, *J. Electrochem. Soc.* **2022**, *169*, 030502.

[65] B. Trang, Y. Li, X.-S. Xue, M. Ateia, K. N. Houk, W. R. Dichtel, *Science* **2022**, *377*, 839.

[66] N.-W. Li, Y. Shi, Y.-X. Yin, X.-X. Zeng, J.-Y. Li, C.-J. Li, L.-J. Wan, R. Wen, Y.-G. Guo, *Angew. Chem., Int. Ed.* **2018**, *57*, 1505.

[67] W. Jia, Q. Wang, J. Yang, C. Fan, L. Wang, J. Li, *ACS Appl. Mater. Interfaces* **2017**, *9*, 7068.

[68] R. Jung, R. Morasch, P. Karayaylali, K. Phillips, F. Maglia, C. Stinner, Y. Shao-Horn, H. A. Gasteiger, *J. Electrochem. Soc.* **2018**, *165*, A132.

[69] J. Bi, J.-C. Lee, H. Liu, *Energies* **2022**, *15*, 2448.

[70] H. Liu, I. H. Naqvi, F. Li, C. Liu, N. Shafiei, Y. Li, M. Pecht, *J. Energy Storage* **2020**, *29*, 101342.

[71] M. U. Tahir, A. Sangwongwanich, D.-I. Stroe, F. Blaabjerg, *J. Energy Chem.* **2023**, *84*, 228.

[72] K. Ku, S.-B. Son, J. Gim, J. Park, Y. Liang, A. Stark, E. Lee, J. Libera, *J. Mater. Chem. A* **2021**, *10*, 288.

[73] N. Anansuksawat, T. Sangsanit, S. Prempluem, K. Homlamai, W. Tejangkura, M. Sawangphruk, *Chem. Sci.* **2024**, *15*, 2026.

[74] J. U. Choi, N. Voronina, Y.-K. Sun, S.-T. Myung, *Adv. Energy Mater.* **2020**, *10*, 2002027.

[75] L. Noerochim, S. Suwarno, N. H. Idris, H. K. Dipojono, *Batteries* **2021**, *7*, 84.

[76] J. Sicklinger, M. Metzger, H. Beyer, D. Pritzl, H. A. Gasteiger, *J. Electrochem. Soc.* **2019**, *166*, A2322.

[77] A. Smith, P. Stüble, L. Leuthner, A. Hofmann, F. Jeschull, L. Mereacre, *Batteries Supercaps* **2023**, *6*, 202300080.

[78] Right from the beginning of the cycling, the cell voltage of pristine cells is fluctuating over a long period of time without reaching the upper voltage limit within the specified time limits (549.59 h; Figure S11, Supporting Information). This behavior indicates the existence of a direct contact between the negative and positive electrode, creating an internal short circuit due to formation of dendritic structures.[108] This direct connection reduces the resistance of the battery system and causes a voltage drop. Afterwards, the voltage is fluctuating to some extent for a certain period even in the

formation cycles, resulting from the current flow through the direct contact and that may be interrupted by the heat generated during the current flow. The interruption can enable a certain recovery of the voltage. This process may occur several times until the voltage limits are reached or charging time exceeds its limit.[109,110] Another consequence of the fluctuating voltage behaviour are the massively increased charge capacities of the cells, which achieve values of two orders above the theoretical capacities.

[79] C. Armbruster, I. Krossing, M. Sellin, M. Seiler, T. Würz, F. Oesten, M. Schmucker, T. Sterbak, J. Fischer, V. Radtke, et al., *Nat. Commun.; Preprint; NCOMMS-24-08896A* **2024**.

[80] E. R. Logan, E. M. Tonita, K. L. Gering, J. Li, X. Ma, L. Y. Beaulieu, J. R. Dahn, *J. Electrochem. Soc.* **2018**, *165*, A21.

[81] I. Krossing, I. Raabe, *Angew. Chem.* **2004**, *116*, 2116.

[82] I. Krossing, A. Reisinger, *Coord. Chem. Rev.* **2006**, *250*, 2721.

[83] N. Kumar, J. M. Seminario, *J. Phys. Chem. C* **2016**, *120*, 16322.

[84] K. Yuan, H. Bian, Y. Shen, B. Jiang, J. Li, Y. Zhang, H. Chen, J. Zheng, *J. Phys. Chem. B* **2014**, *118*, 3689.

[85] T. Hou, K. D. Fong, J. Wang, K. A. Persson, *Chem. Sci.* **2021**, *12*, 14740.

[86] A. J. Ringsby, K. D. Fong, J. Self, H. K. Bergstrom, B. D. McCloskey, K. A. Persson, *J. Electrochem. Soc.* **2021**, *168*, 080501.

[87] S. A. Krachkovskiy, J. D. Bazak, S. Fraser, I. C. Halalay, G. R. Goward, *J. Electrochem. Soc.* **2017**, *164*, A912.

[88] Q. Liu, A. Cresce, M. Schroeder, K. Xu, D. Mu, B. Wu, L. Shi, F. Wu, *Energy Storage Mater.* **2019**, *17*, 366.

[89] Y. Yamada, A. Yamada, *J. Electrochem. Soc.* **2015**, *162*, A2406.

[90] Q. Zhao, S. Stalin, L. A. Archer, *Joule* **2021**, *5*, 1119.

[91] S. Yuan, T. Kong, Y. Zhang, P. Dong, Y. Zhang, X. Dong, Y. Wang, Y. Xia, *Angew. Chem., Int. Ed.* **2021**, *60*, 25624.

[92] G. Yang, Y. Li, S. Liu, S. Zhang, Z. Wang, L. Chen, *Energy Storage Mater.* **2019**, *23*, 350.

[93] Z. Hao, G. Li, Y. Lu, Y. Cai, G. Yang, J. Chen, *Nano Res.* **2023**, *16*, 12647.

[94] S.-T. Hong, J.-S. Kim, S.-J. Lim, W. Y. Yoon, *Electrochim. Acta* **2004**, *50*, 535.

[95] R. Miao, J. Yang, Z. Xu, J. Wang, Y. Nuli, L. Sun, *Sci. Rep.* **2016**, *6*, 21771.

[96] D. Lu, Y. Shao, T. Lozano, W. D. Bennett, G. L. Graff, B. Polzin, J. Zhang, M. H. Engelhard, N. T. Saenz, W. A. Henderson, P. Bhattacharya, J. Liu, J. Xiao, *Adv. Energy Mater.* **2015**, *5*, 1400993.

[97] The investigated electrodes were extracted from the full cells or symmetrical cells, which can lead to a mechanical impact on the thin electrode foils. The extent of the impact is difficult to assess since the electrodes were also cut with a scalpel.

[98] A. Mauger, C. M. Julien, *Inorganics* **2022**, *10*, 5.

[99] S.-K. Otto, Y. Moryson, T. Krauskopf, K. Peppler, J. Sann, J. Janek, A. Henss, *Chem. Mater.* **2021**, *33*, 859.

[100] a) K. Kanamura, H. Tamura, S. Shiraishi, Z. Takehara, *J. Electrochem. Soc.* **1995**, *142*, 340; b) M. L. Meyerson, J. K. Sheavly, A. Dolocan, M. P. Griffin, A. H. Pandit, R. Rodriguez, R. M. Stephens, D. A. Vanden Bout, A. Heller, C. B. Mullins, *J. Mater. Chem. A* **2019**, *7*, 14882; c) K. Morigaki, A. Ohta, *J. Power Sources* **1998**, *76*, 159; d) C. Naudin, J. L. Bruneel, M. Chami, B. Desbat, J. Grondin, J. C. Lassègues, L. Servant, *J. Power Sources* **2003**, *124*, 518.

[101] J. P. Schmidt, T. Chrobak, M. Ender, J. Illig, D. Klotz, E. Ivers-Tiffée, *J. Power Sources* **2011**, *196*, 5342.

[102] M. Gaberscek, J. Moskon, B. Erjavec, R. Dominko, J. Jamnik, *Electrochem. Solid-State Lett.* **2008**, *11*, A170.

[103] J. Landesfeind, D. Pritzl, H. A. Gasteiger, *J. Electrochem. Soc.* **2017**, *164*, A1773.

[104] J. Illig, M. Ender, A. Weber, E. Ivers-Tiffée, *J. Power Sources* **2015**, *282*, 335.

[105] M. Srout, M. Carboni, J.-A. Gonzalez, S. Trabesinger, *Small* **2023**, *19*, 2206252.

[106] N. Ogihara, S. Kawauchi, C. Okuda, Y. Itou, Y. Takeuchi, Y. Ukyo, *J. Electrochem. Soc.* **2012**, *159*, A1034.

[107] D. Pritzl, A. E. Bumberger, M. Wetjen, J. Landesfeind, S. Solchenbach, H. A. Gasteiger, *J. Electrochem. Soc.* **2019**, *166*, A582.

[108] G. Homann, L. Stolz, J. Nair, I. C. Laskovic, M. Winter, J. Kasnatscheew, *Sci. Rep.* **2020**, *10*, 4390.

[109] R. Zhu, J. Feng, Z. Guo, *J. Electrochem. Soc.* **2019**, *166*, A1107.

[110] S. Menkin, J. B. Fritzke, R. Larner, C. de Leeuw, Y. Choi, A. B. Gunnarsdóttir, C. P. Grey, *Faraday Discuss.* **2023**, *248*, 277.